Cell Reports

Article

Skeletal progenitors preserve proliferation and self-renewal upon inhibition of mitochondrial respiration by rerouting the TCA cycle

Graphical abstract

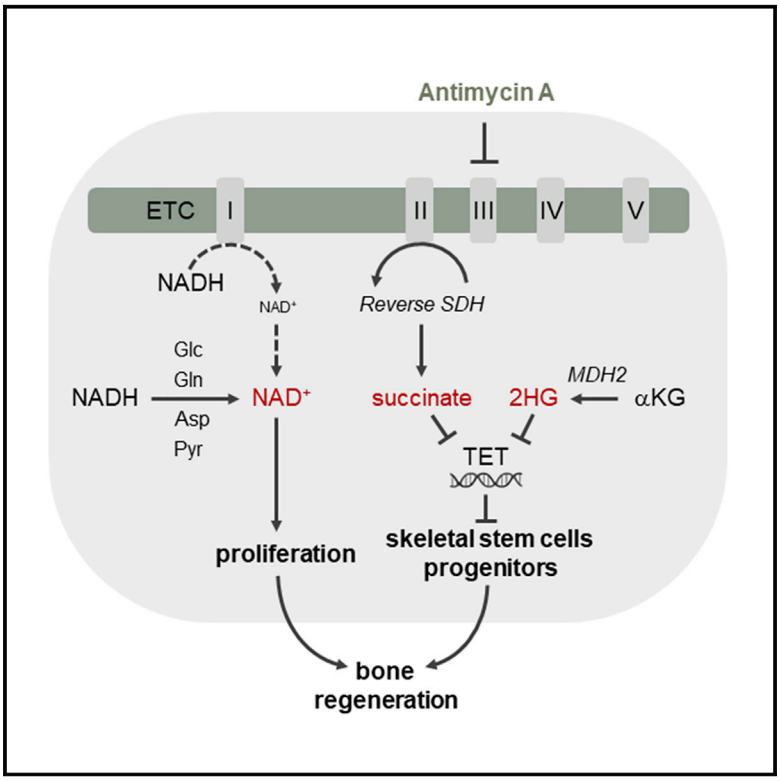

Authors

Guillaume Tournaire, Shauni Loopmans, Steve Stegen, ..., Sarah-Maria Fendt, Nick van Gastel, Geert Carmeliet

Correspondence

geert.carmeliet@kuleuven.be

In brief

Blocking mitochondrial respiration decreases proliferation in tumor cells but not in stem cells, although mechanistic insight is lacking. Tournaire et al. report that skeletal progenitors bypass this inhibition by reversing succinate dehydrogenase activity and using alternative NAD^+ regenerating pathways. This metabolic plasticity maintains proliferation and self-renewal, improving bone regeneration.

Highlights

- Skeletal stem/progenitor cells can proliferate upon electron transport chain blockade
- Succinate dehydrogenase is reversed with fumarate functioning as electron acceptor
- Pyruvate and aspartate are critical for NAD^+ regeneration and proliferation
- Metabolic changes prevent DNA demethylation and preserve self-renewal

Tournaire et al., 2022, Cell Reports *40*, 111105
July 26, 2022
https://doi.org/10.1016/j.celrep.2022.111105

CellPress

Cell Reports

CellPress
OPEN ACCESS

Article

Skeletal progenitors preserve proliferation and self-renewal upon inhibition of mitochondrial respiration by rerouting the TCA cycle

Guillaume Tournaire,[1,2] Shauni Loopmans,[1,2] Steve Stegen,[1,2] Gianmarco Rinaldi,[3,4] Guy Eelen,[5,6] Sophie Torrekens,[1] Karen Moermans,[1] Peter Carmeliet,[5,6] Bart Ghesquière,[7] Bernard Thienpont,[8] Sarah-Maria Fendt,[3,4] Nick van Gastel,[9] and Geert Carmeliet[1,2,10,*]

[1]Laboratory of Clinical and Experimental Endocrinology, Department of Chronic Diseases and Metabolism, KU Leuven, O&N1bis Herestraat 49, 3000 Leuven, Belgium
[2]Prometheus, Division of Skeletal Tissue Engineering, KU Leuven, Leuven, Belgium
[3]Laboratory of Cellular Metabolism and Metabolic Regulation, VIB Center for Cancer Biology, Leuven, Belgium
[4]Laboratory of Cellular Metabolism and Metabolic Regulation, Department of Oncology and Leuven Cancer Institute, KU Leuven, Leuven, Belgium
[5]Laboratory of Angiogenesis and Vascular Metabolism, VIB Center for Cancer Biology, Leuven, Belgium
[6]Laboratory of Angiogenesis and Vascular Metabolism, Department of Oncology and Leuven Cancer Institute, KU Leuven, Leuven, Belgium
[7]Metabolomics Expertise Center, Department of Oncology, KU Leuven/VIB Center for Cancer Biology Leuven, Leuven, Belgium
[8]Laboratory of Functional Epigenetics, Department of Human Genetics, KU Leuven, Leuven, Belgium
[9]de Duve Institute, UC Louvain, Brussels, Belgium
[10]Lead contact
*Correspondence: geert.carmeliet@kuleuven.be
https://doi.org/10.1016/j.celrep.2022.111105

SUMMARY

A functional electron transport chain (ETC) is crucial for supporting bioenergetics and biosynthesis. Accordingly, ETC inhibition decreases proliferation in cancer cells but does not seem to impair stem cell proliferation. However, it remains unclear how stem cells metabolically adapt. In this study, we show that pharmacological inhibition of complex III of the ETC in skeletal stem and progenitor cells induces glycolysis side pathways and reroutes the tricarboxylic acid (TCA) cycle to regenerate NAD^+ and preserve cell proliferation. These metabolic changes also culminate in increased succinate and 2-hydroxyglutarate levels that inhibit Ten-eleven translocation (TET) DNA demethylase activity, thereby preserving self-renewal and multilineage potential. Mechanistically, mitochondrial malate dehydrogenase and reverse succinate dehydrogenase activity proved to be essential for the metabolic rewiring in response to ETC inhibition. Together, these data show that the metabolic plasticity of skeletal stem and progenitor cells allows them to bypass ETC blockade and preserve their self-renewal.

INTRODUCTION

By transporting electrons from different sources to the final electron acceptor oxygen, the mitochondrial electron transport chain (ETC) is involved not only in bioenergetics but also in biosynthetic processes. Indeed, by accepting electrons from NADH, complex I of the ETC supports the regeneration of NAD^+, a co-factor used as electron acceptor in several metabolic pathways such as nucleotide and amino acid synthesis (Birsoy et al., 2015; Lunt and Vander Heiden, 2011; Sullivan et al., 2015; Vasan et al., 2020). Similarly, complex II transfers electrons from $FADH_2$ via ubiquinone to oxygen, but it is also directly linked to the tricarboxylic acid (TCA) cycle by converting succinate to fumarate via its succinate dehydrogenase (SDH) subunit. In addition, the ETC supports a crucial step in pyrimidine synthesis, as ubiquinone accepts electrons from dihydroorotate dehydrogenase (DHODH), when dihydroorotate is converted to orotate. Ubiquinone thus receives electrons from complex I, complex II, and DHODH, resulting in the generation of ubiquinol, which is oxidized back to ubiquinone by complex III. These pleiotropic functions of the ETC likely explain the proliferation defect observed in cancer and endothelial cells upon ETC inhibition (Birsoy et al., 2015; Diebold et al., 2019; Diehl et al., 2019; Sullivan et al., 2015). In contrast, blocking ETC complex III in stem cells, such as embryonic or hematopoietic stem cells, does not reduce proliferation but changes their differentiation potential (Anso et al., 2017; Pereira et al., 2013; Varum et al., 2009). These findings suggest a greater metabolic plasticity of stem cells compared with cancer cells, although it remains unknown how stem cells bypass ETC inhibition to ensure proliferation.

Skeletal stem and progenitor cells (SSPCs) are self-renewing cells found in bone marrow, growth plate, and periosteum, and can give rise to chondrocytes, osteoblasts, adipocytes, and hematopoiesis-supportive stromal cells (Bianco et al., 2013;

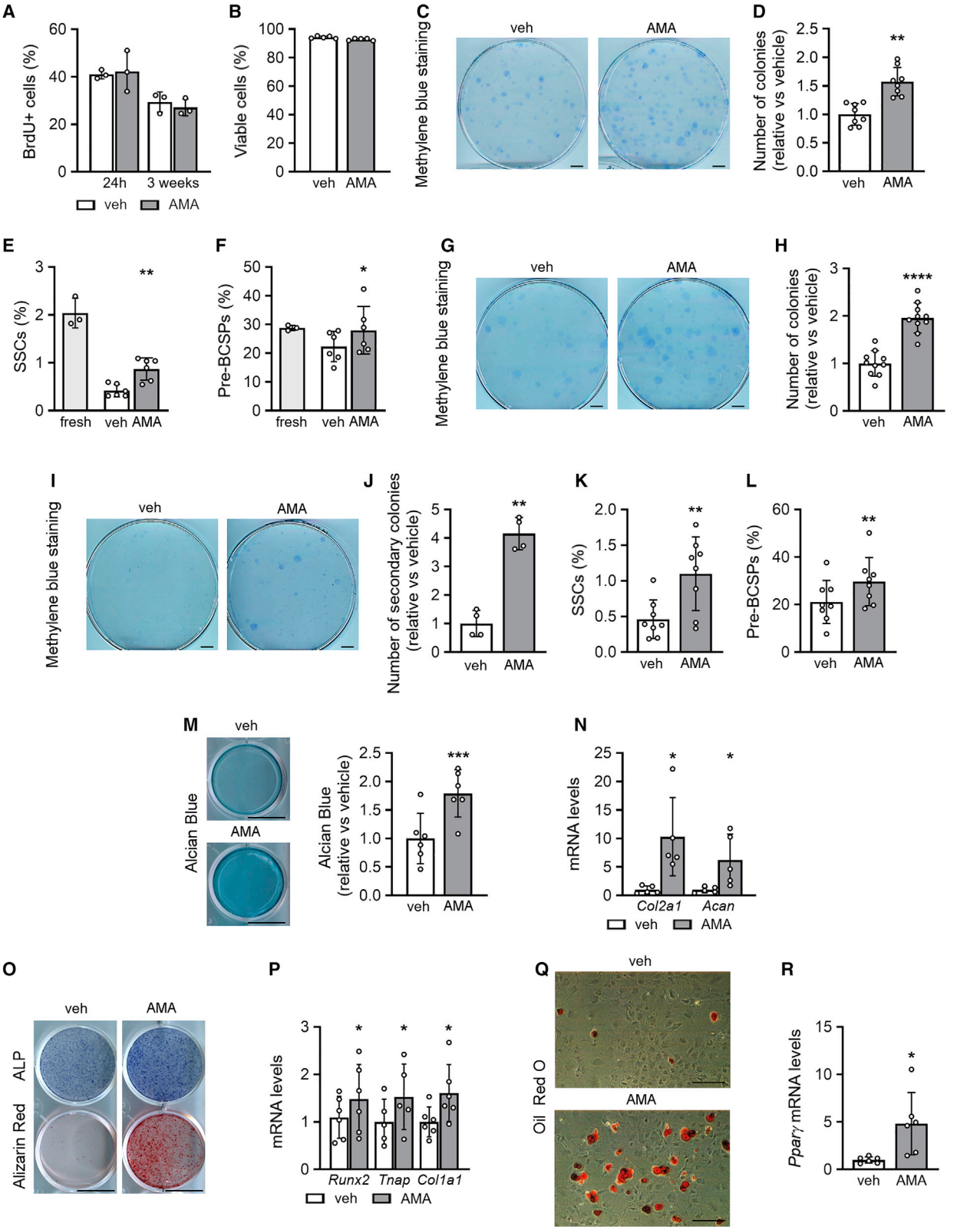

(legend on next page)

Chan et al., 2015; Sacchetti et al., 2007). Periosteal SSPCs are crucial for bone repair (Colnot, 2009; Zhang et al., 2005) and start to proliferate and differentiate in an avascular milieu, suggesting that SSPCs, similar to other stem cell types, exhibit metabolic plasticity to adapt and proliferate in a challenging environment.

In this study, we used SSPCs as a model to investigate the metabolic flexibility of stem cells upon ETC inhibition. We show that when ETC complex III is inhibited, extensive metabolic rewiring at the level of the TCA cycle, primarily through reverse SDH activity, in combination with NAD^+ regenerating pathways, allows SSPCs to expand and preserve their multilineage potential. These findings provide mechanistic insight into the metabolic plasticity of adult stem cell populations and support the development of metabolic strategies to improve cell-based regenerative medicine.

RESULTS

SSPCs preserve proliferation, self-renewal, and trilineage potential upon ETC dysfunction

To confirm our hypothesis that cancer and stem cells respond differently to ETC inhibition, we analyzed the effect of the ETC complex III inhibitor antimycin A (AMA) on the proliferation of four cancer cell types versus mouse periosteal-derived cells (mPDCs), a cell source rich in SSPCs. Of note, all cells were cultured in the same medium, containing glucose (5.5 mM), pyruvate (1 mM), glutamine (2 mM), and aspartate (0.22 mM). AMA treatment decreased the proliferation of tumor cells (Figures S1A and S1B) but did not affect proliferation nor survival of mPDCs (Figures 1A and 1B). However, mPDCs showed a marked decrease in oxygen consumption upon AMA treatment (Figure S1C), indicating that these cells have a functional ETC and can metabolically adapt to ETC blockade. The ability to sustain proliferation was specific for SSPCs, as AMA treatment reduced proliferation of lineage-committed skeletal cells, such as mouse growth plate chondrocytes and mature osteoblasts, differentiated from calvarial osteoprogenitors (Figures S1D–S1J). Thus, the capacity to ensure proliferation upon mitochondrial complex III blockade is specific for SSPCs and absent in lineage-committed skeletal cells.

To verify that the positive effect on proliferation did not exhaust SSPC properties, we used three approaches: colony formation, flow-cytometry-based analysis of SSPC markers (Chan et al., 2015), and trilineage differentiation potential (Figure S1K, short protocol). First, AMA-treated cells generated more colonies than vehicle-treated cells (Figures 1C and 1D). Second, using described stem and progenitor markers, we observed that the stromal fraction of freshly isolated mPDCs contained 2.04% ± 0.31% skeletal stem cells (SSCs; $CD31^-/CD45^-/Ter119^-/CD51^+/CD90^-/CD105^-/BP1^-/CD200^+$; n = 3; mean ± SD), 28.79% ± 0.93% pre-bone, cartilage, and stromal progenitors (pre-BCSPs; $CD31^-/CD45^-/Ter119^-/CD51^+/CD90^-/CD105^-/BP1^-/CD200^-$; n = 3; mean ± SD), and the rest were more lineage-restricted skeletal progenitors. After 1 week of culture, 75% of SSCs and 20% of pre-BCSPs were lost in vehicle-treated mPDCs, whereas AMA treatment preserved these populations (Figures 1E and 1F). Third, treating mPDCs seeded at colony-forming density with AMA for 10 days resulted in a higher number of colonies (Figures S1K, S2A, and S2B). Switching to differentiation medium, in the absence of AMA, induced a higher proportion of colonies to differentiate to the chondrogenic (Alcian blue staining), osteogenic (alkaline phosphatase [ALP] activity), and adipogenic (oil red O staining; Figures S2C and S2D) lineage, indicating that AMA treatment preserves the trilineage potential of SSPCs and prevents their exhaustion after cell expansion.

Similar to the short regimen, long-term treatment of mPDCs with AMA preserved proliferation (Figure S1K [long protocol] and Figure 1A) and SSPC characteristics, as evidenced by the increase in primary and secondary colonies (Figures 1G–1J), the higher percentage of SSCs (1.1% ± 0.52% versus 0.46% ± 0.27%, AMA versus vehicle) and pre-BCSPs (29.63% ± 10.11% versus 21.07% ± 9.06%, AMA versus vehicle; Figures 1K and 1L) and increased trilineage potential (Figures 1M–1R). Of note, while SSPCs expanded with AMA maintained their multipotency, AMA treatment during differentiation decreased the trilineage potential (Figures S2E–S2J), suggesting that ETC function is required for SSPC differentiation. To exclude that these findings are AMA specific, we confirmed that another inhibitor of mitochondrial complex III, myxothiazol (Myx), had no effect on proliferation or survival but increased SSPC properties (Figures S2K–S2O).

Figure 1. SSPCs preserve proliferation, self-renewal, and trilineage potential upon ETC dysfunction

(A) Flow-cytometry analysis of BrdU-positive ($BrdU^+$) mouse periosteal cells (mPDCs) treated for 24 h or 3 weeks with vehicle (veh) or 10 μM antimycin A (AMA) (n = 3).

(B) Cell viability of veh- and AMA-treated mPDCs, analyzed by annexin V-propidium iodide flow cytometry (n = 5).

(C and D) Visualization (methylene blue staining) and quantification of primary colonies, formed by mPDCs treated with veh or AMA for 1 week (n = 8).

(E) Flow-cytometry analysis of the percentage of skeletal stem cells (SSCs) in freshly isolated mPDCs (fresh) or after treatment with veh or AMA for 1 week (n = 6).

(F) Flow-cytometry analysis of the percentage of pre-bone, cartilage, and stromal progenitors (pre-BCSP) in freshly isolated mPDCs or after treatment with veh or AMA for 1 week (n = 6).

(G–J) Visualization (methylene blue staining) and quantification of primary (G and H; n = 10) and secondary (I and J; n = 4) colonies, formed by mPDCs treated with veh or AMA for 3 weeks.

(K and L) Flow-cytometry analysis of the percentage of SSCs (K) and pre-BCSPs (L) in mPDCs treated with veh or AMA for 3 weeks (n = 8).

(M and N) Chondrogenic differentiation of mPDCs treated with veh or AMA for 3 weeks and assessed by visualization and quantification of chondrogenic matrix (Alcian blue staining; M, n = 6) and *Col2a1* and *Acan* mRNA levels (N, n = 5).

(O and P) Osteogenic differentiation of mPDCs treated with veh or AMA for 3 weeks and assessed by staining for alkaline phosphatase activity (ALP) and mineralized matrix (Alizarin red staining; O, n = 5) and quantification of *Runx2*, *Tnap*, and *Col1a1* mRNA levels (P, n = 5–6).

(Q and R) Adipogenic differentiation of mPDCs treated with veh or AMA for 3 weeks and assessed by visualization of lipid deposits (oil red O staining; Q, n = 10) and quantification of *Pparγ* mRNA levels (R, n = 6).

Data are means ± SD. *p < 0.05, **p < 0.01, ***p < 0.001, ****p < 0.0001 versus vehicle (paired two-tailed Student's t test). Scale bars, 1 cm (C, G, I, M, O) and 200 μm (Q). See also Figures S1 and S2.

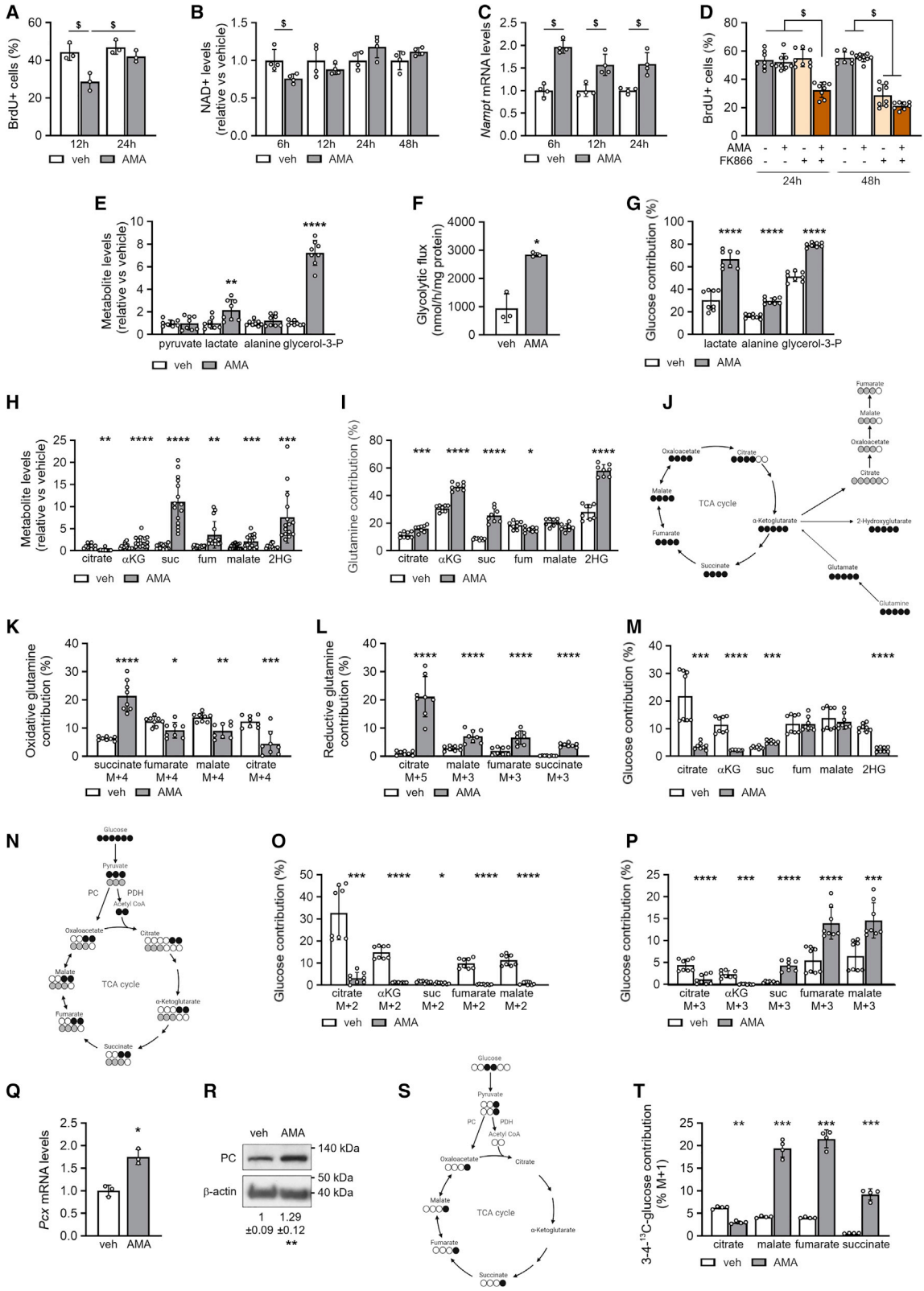

(legend on next page)

Thus, SSPCs preserve proliferation and self-renewal when ETC complex III is blocked.

SSPCs increase the NAD(H) pool to preserve proliferation when ETC is inhibited

The normal proliferation of SSPCs upon AMA treatment (Figure 1A) suggests that SSPCs have a high metabolic plasticity to sustain proliferation upon ETC blockade. Indeed, AMA treatment reduced proliferation during the first 12 h, but it was restored again after 24 h (Figure 2A).

To unravel the mechanism behind the metabolic flexibility of SSPCs we first analyzed cellular energy levels, as the ETC is a major source of ATP production. AMA treatment resulted in an energy deficit as evidenced by reduced energy charge, increased AMP/ATP ratio, and higher levels of activated AMPK (p-AMPK^{T172}) (Figures S3A–S3C). Despite this energy deficit, cell proliferation of SSPCs was normal, suggesting that the energy deficit did not restrict proliferation.

Research in tumor cells has revealed that ETC inhibition can reduce proliferation because of impaired conversion of NADH to NAD$^+$ at complex I, resulting in decreased NAD$^+$ levels (Diehl et al., 2019; Gui et al., 2016; Luengo et al., 2020). By blocking complex III of the ETC, AMA may indirectly inhibit the electron transport from complex I, thereby reducing NAD$^+$ regeneration (Fendt et al., 2013) (Figures S3I and S3J). NAD$^+$ levels are linked to proliferation, as this co-factor is critical for the synthesis of oxidized macromolecules such as nucleotides and amino acids (Bao et al., 2016; Birsoy et al., 2015; Diehl et al., 2019; Garcia-Bermudez et al., 2018; Gui et al., 2016; Sullivan et al., 2015), and NAD$^+$ is also required for histone deacetylation by sirtuins and for poly(ADP-ribose) polymerase activity (Kennedy et al., 2016). We observed that NADH levels increased in AMA-treated mPDCs from 6 h on, resulting in a decreased NAD$^+$/NADH ratio (Figures S3D and S3E). Consequently, NAD$^+$ levels decreased briefly upon AMA treatment but, interestingly, were restored to levels similar to or even higher than the ones observed in vehicle-treated cells at 24 h (Figure 2B), resulting in an increased total NAD(H) pool (Figure S3F). In line with these results, NAD$^+$ levels were also preserved after Myx treatment (Figures S3G and S3H). These temporary changes in NAD$^+$ levels correspond to the proliferation dynamics, suggesting a link between maintenance of NAD$^+$ levels and proliferation in AMA-treated SSPCs.

We next investigated how SSPCs preserved NAD$^+$ levels upon ETC blockade. The increase in the total NAD(H) pool upon AMA treatment suggests enhanced NAD synthesis. NAD$^+$ can be synthesized in the salvage pathway, where nicotinamide, released in NAD$^+$-dependent signaling reactions or taken up from the environment, is converted first to nicotinamide mononucleotide by nicotinamide phosphoribosyltransferase (NAMPT) and then to NAD$^+$ (Kennedy et al., 2016; Thapa and Dallmann, 2020). We found increased *Nampt* expression in AMA-treated cells (Figure 2C) and investigated its importance for proliferation by using the NAMPT inhibitor FK866. Adding FK866 for 24 h reduced bromodeoxyuridine (BrdU) incorporation in AMA-treated cells, whereas this decrease was only observed after 48 h in vehicle-treated cells (Figure 2D), indicating that AMA-treated SSPCs rely more on NAD$^+$ synthesis for proliferation.

Together, these data indicate that SSPCs increase the NAD$^+$ pool when mitochondrial respiration is blocked.

Glycerol-3-phosphate biosynthesis contributes to NAD$^+$ regeneration in AMA-treated SSPCs

In addition to NAD$^+$ synthesis, we hypothesized that AMA-treated SSPCs upregulated NAD$^+$ regeneration pathways (Figures S3I and S3J) and focused first on glycolysis and its side pathways. AMA treatment increased glycolysis, as evidenced by increased glucose uptake, lactate levels, and lactate efflux, higher lactate/glucose ratio and glycolytic flux, and enhanced contribution of $^{13}C_6$-glucose to lactate (Figures 2E–2G and S3K–S3M). This increase in glycolysis likely prevented an even larger energy deficit but also caused AMA-treated cells

Figure 2. SSPCs increase NAD(H) pool and NAD$^+$ regeneration by glycolysis side pathway and TCA cycle rerouting

(A) Flow-cytometry analysis of BrdU$^+$ SSPCs treated with vehicle (veh) or 10 μM AMA for 12 h or 24 h (n = 3).
(B) NAD$^+$ levels after treatment for indicated times (n = 4).
(C) *Nampt* mRNA levels after treatment for indicated times (n = 4).
(D) Flow-cytometry analysis of BrdU$^+$ SSPCs treated for 24 h or 48 h with veh or AMA with or without 10 nM FK866 (n = 8).
(E) Metabolite levels of pyruvate, lactate, alanine, and glycerol-3-phosphate (glycerol-3-P) after treatment for 3 days (n = 8).
(F) Glycolytic flux (n = 3).
(G) Fractional contribution of $^{13}C_6$-glucose to lactate, alanine, and glycerol-3-P (n = 8).
(H) Metabolite levels of citrate, α-ketoglutarate (αKG), succinate (suc), fumarate (fum), malate, and 2-hydroxyglutarate (2HG) after treatment for 3 days (n = 11–15).
(I) Fractional contribution of $^{13}C_5$-glutamine to citrate, αKG, suc, fum, malate, and 2HG (n = 8).
(J) Schematic representation of $^{13}C_5$-glutamine labeling patterns. Empty circles indicate ^{12}C, black circles denote ^{13}C derived from oxidative metabolism, and gray circles denote ^{13}C derived from reductive metabolism.
(K and L) Oxidative (K) and reductive (L) contribution of $^{13}C_5$-glutamine to suc, fum, malate, and citrate (n = 8).
(M) Fractional contribution of $^{13}C_6$-glucose to citrate, αKG, suc, fum, malate, and 2HG (n = 8).
(N) Schematic representation of $^{13}C_6$-glucose labeling patterns. Empty circles indicate ^{12}C, black circles denote ^{13}C entering TCA cycle via pyruvate dehydrogenase (PDH), and gray circles denote ^{13}C entering TCA cycle via pyruvate carboxylase (PC).
(O and P) M + 2 (O) and M + 3 (P) contribution of $^{13}C_6$-glucose to citrate, αKG, suc, fum, and malate (n = 8).
(Q and R) *Pcx* mRNA levels (Q, n = 3) and immunoblot detection of PC and β-actin (R). Representative image of three experiments is shown.
(S) Schematic representation of [3,4]-$^{13}C_2$-glucose labeling of TCA cycle intermediates. Empty circles indicate ^{12}C, black circles denote ^{13}C entering TCA cycle via PC activity.
(T) M + 1 contribution of [3,4]-$^{13}C_2$-glucose to citrate, malate, fum, and suc.
Data are means ± SD. *p < 0.05, **p < 0.01, ***p < 0.001, ****p < 0.0001 versus veh-treated cells (paired two-tailed Student's t test), $^{\$}$p < 0.05 (two-way ANOVA). See also Figure S3.

to become highly dependent on extracellular glucose as glucose deprivation for 24 h reduced their survival (Figure S3N).

Next to increased glycolysis, we observed adaptations in side pathways of glycolysis upon AMA treatment, as $^{13}C_6$-glucose contributed more to glycerol-3-phosphate (glycerol-3-P) and alanine, which was associated with a manifest increase in glycerol-3-P levels (Figures 2E and 2G). The conversion of the glycolysis intermediate dihydroxyacetone phosphate to glycerol-3-P by glycerol-3-P dehydrogenase (GPDH) involves the oxidation of NADH to NAD^+, and thus contributes to NAD^+ regeneration, as recently reported (Figure S3J) (Liu et al., 2021). The synthesis of alanine from pyruvate via transamination converts simultaneously glutamate to α-ketoglutarate (αKG) and can thus bypass glutamate dehydrogenase, which needs NAD^+ as co-factor. However, this transaminase reaction consumes pyruvate that could otherwise be converted to lactate and regenerate NAD^+.

Thus, the increase in the glycerol-3-P pathway likely contributes to NADH/NAD^+ redox homeostasis by increasing NAD^+ regeneration.

Rerouting of the TCA cycle and reverse SDH activity in AMA-treated cells

As the TCA cycle is a major source of NADH production (Figure S3I) and the electron transfer from NADH to complex I of the ETC is indirectly inhibited by AMA, we expected a decrease in the levels of TCA cycle intermediates in AMA-treated SSPCs. We found reduced citrate levels (−80%), but an increase in αKG (2-fold), malate (2-fold), fumarate (3-fold), and especially succinate (11-fold), as well as in the αKG derivative 2HG (8-fold) (Figure 2H).

To understand these unexpected changes in TCA cycle metabolites, we analyzed glutamine and glucose metabolism, two important nutrients for TCA cycle activity in SSPCs (Figure S3O). Glutamine uptake was not changed (Figure S3P), but the contribution of $^{13}C_5$-glutamine to αKG, and especially to succinate, was increased in AMA-treated cells (Figure 2I). More precisely, the oxidative contribution of $^{13}C_5$-glutamine to $^{13}C_4$-succinate was increased, but the contribution to $^{13}C_4$-fumarate, $^{13}C_4$-malate, and $^{13}C_4$-citrate was decreased in AMA-treated cells (Figures 2J and 2K), indicating a block of succinate oxidation. It is likely that SDH is indirectly inhibited, as it is part of ETC complex II and cannot further transfer electrons to complex III upon AMA treatment (Vasan et al., 2020) (Figure S3J). However, reductive carboxylation of $^{13}C_5$-glutamine was strongly increased in AMA-treated cells with higher contribution to $^{13}C_5$-citrate, $^{13}C_3$-malate, and $^{13}C_3$-fumarate (Figure 2L). Surprisingly, we also detected $^{13}C_3$-succinate in AMA-treated cells but none in controls, suggesting conversion of fumarate to succinate and thus reversal of SDH activity (Figure 2L). $^{13}C_5$-glutamine also contributed more to 2HG upon AMA treatment (Figure 2I). These changes in glutamine metabolism in AMA-treated SSPCs can contribute to NADH/NAD^+ balance as follows: first, less NADH is produced in the TCA cycle as the oxidative arm is partially blocked at SDH, leading to decreased conversion of malate to oxaloacetate (OAA); and second, NAD^+ is regenerated by the increase in reductive carboxylation flux, with conversion of OAA to malate and by the enhanced conversion of αKG to 2HG (Figure S3J).

Oxidative glucose metabolism was also altered upon AMA treatment, as the contribution of $^{13}C_6$-glucose to citrate and αKG was decreased, whereas its contribution to malate and fumarate was similar and to succinate even increased (Figure 2M), suggesting altered entry and/or metabolism of glucose in the TCA cycle. $^{13}C_6$-glucose-derived pyruvate can enter the TCA cycle either via pyruvate dehydrogenase (PDH) that decarboxylates $^{13}C_3$-pyruvate to $^{13}C_2$-acetyl-coenzyme A (CoA) (M + 2 labeling), or via pyruvate carboxylase (PC) that adds an unlabeled CO_2 to $^{13}C_3$-pyruvate to form four-carbon $^{13}C_3$-OAA (M + 3 labeling; Figure 2N). We found that M + 2 labeling of citrate, αKG, succinate, malate, and fumarate was manifestly decreased upon AMA treatment (Figure 2O), indicative of decreased PDH-mediated TCA cycle anaplerosis. On the other hand, M + 3 labeling of malate, fumarate, and succinate was increased whereas M + 3 labeling of citrate and αKG was decreased (Figure 2P), suggesting that glucose enters the TCA cycle through PC and is then converted not to citrate and αKG but to malate, fumarate, and succinate (Figure S3J).

The enhanced PC activity in AMA-treated cells was further confirmed by increased PC mRNA and protein levels (Figures 2Q and 2R), and by [3,4]-$^{13}C_2$-glucose tracing. This approach labels glucose-derived pyruvate M + 1 and can only label TCA cycle intermediates when pyruvate is metabolized via PC, as the ^{13}C label is lost when pyruvate is converted via PDH prior to entering the TCA cycle (Figure 2S). This method also excludes the possibility that $^{13}C_6$-glucose-derived M + 3 labeling is due to a second TCA turn. We found that M + 1 labeling of malate, fumarate, and succinate was increased in AMA-treated cells and that M + 1 citrate labeling was decreased (Figure 2T), proving that PC activity is increased.

This rerouted glucose metabolism in the TCA cycle contributes to NAD^+ levels in two ways (Figure S3J). First, the conversion of glucose-derived pyruvate to OAA via PC and not to acetyl-CoA through PDH allows glucose to enter the TCA cycle without consuming NAD^+ in the PDH-mediated reaction. Second, OAA is not converted to αKG via citrate, thus reducing NAD^+ consumption in the TCA cycle. Rather, OAA is metabolized to malate by malate dehydrogenase (MDH), which regenerates NAD^+ instead of producing NADH. These data show that, next to glutamine, glucose is metabolized to succinate by reverse SDH activity in AMA-treated SSPCs, indicating that fumarate is acting as an electron acceptor receiving electrons from ubiquinol. The reverse SDH activity will thus allow some electron transfer from complex I and conversion of NADH to NAD^+.

Extracellular pyruvate promotes glucose-metabolizing pathways that regenerate NAD^+

In tumor cells, the decrease in proliferation by ETC inhibition can be rescued by increasing extracellular pyruvate that functions as an electron acceptor when converted to lactate by lactate dehydrogenase (LDH) (Gui et al., 2016; Sullivan et al., 2015). Similar to tumor cells, $^{13}C_3$-pyruvate was mainly metabolized to lactate, thereby converting NADH to NAD^+, and minimally to malate and citrate in AMA-treated SSPCs (Figure 3A). However, pyruvate deprivation further reduced the proliferation of AMA-treated tumor cells (Figures S4A–S4H), whereas it had no effect on proliferation, or on NAD^+ levels, of AMA-treated SSPCs (Figures 3G and 3H).

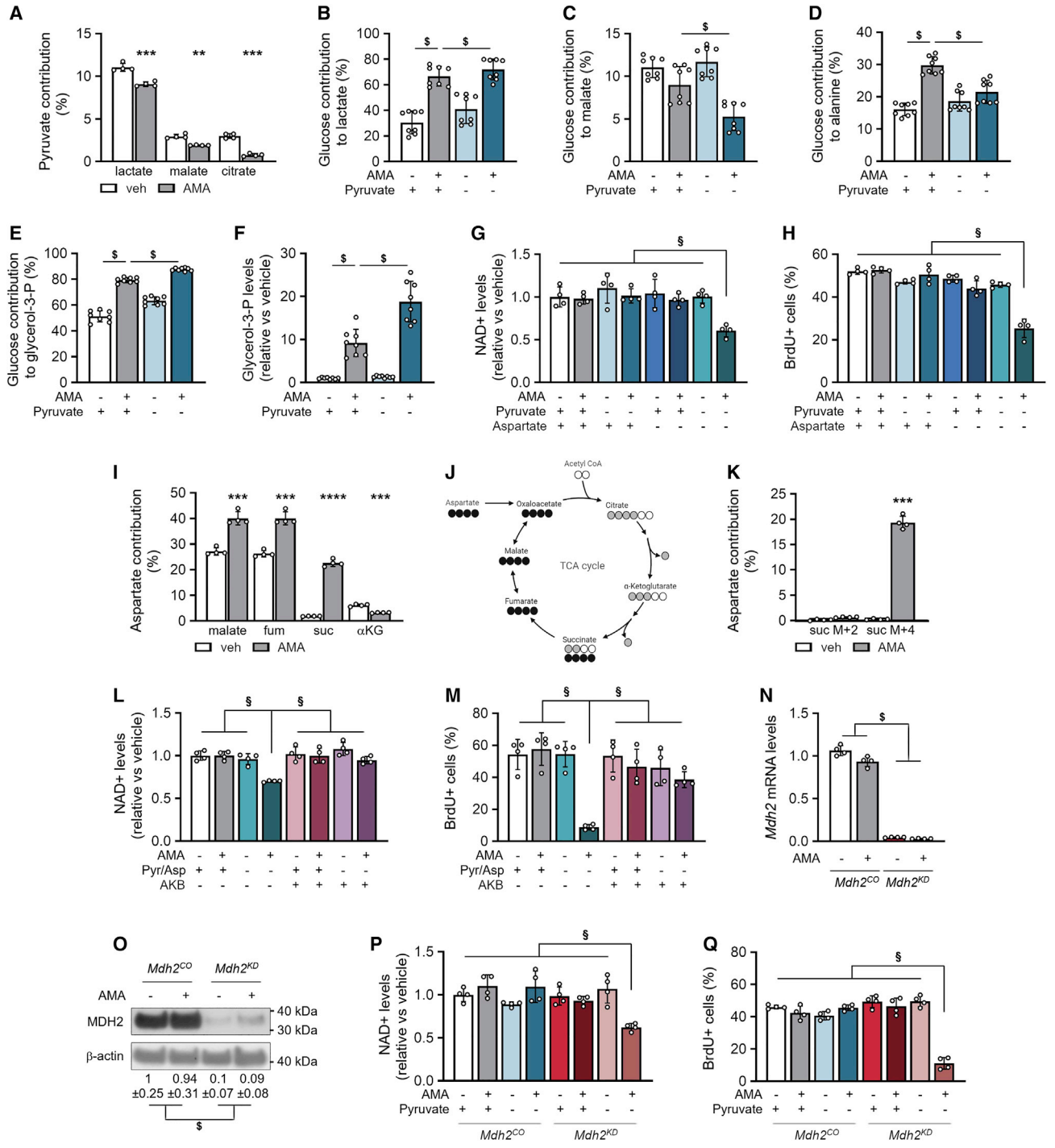

Figure 3. Extracellular pyruvate and MDH2 control NAD$^+$ regeneration

(A) Fractional contribution of $^{13}C_3$-pyruvate to lactate, malate, and citrate in cells treated with vehicle (veh) or 10 μM AMA for 3 days (n = 4).

(B–E) Fractional contribution of $^{13}C_6$-glucose to lactate (B, n = 8), malate (C, n = 8), alanine (D, n = 8) and glycerol-3-phosphate (glycerol-3-P; E, n = 8) in cells cultured with or without 1 mM pyruvate.

(F) Glycerol-3-P levels in cells cultured with or without pyruvate (n = 8).

(G) NAD$^+$ levels in cells cultured in either full medium (1 mM pyruvate, 0.22 mM aspartate) or without pyruvate, aspartate, or combination (n = 4).

(H) Flow-cytometry analysis of BrdU$^+$ cells cultured in either full medium or without pyruvate, aspartate, or combination (n = 4).

(I) Fractional contribution of $^{13}C_4$-aspartate to malate, fumarate (fum), succinate (suc), and α-ketoglutarate (αKG) after treatment for 3 days (n = 4).

(legend continued on next page)

We hypothesized that AMA-treated SSPCs preserve NAD^+/NADH balance upon pyruvate withdrawal by adapting glucose and/or glutamine metabolism. Pyruvate deprivation of AMA-treated cells caused $^{13}C_6$-glucose to contribute more to lactate and less to malate and alanine (Figures 3B–3D). The decreased alanine transaminase activity reduced not only alanine secretion but also the contribution of $^{13}C_5$-glutamine to αKG and 2HG, resulting in decreased αKG and 2HG levels (Figures S5A–S5D). Of note, malate levels were not significantly changed in pyruvate-deprived AMA-treated cells (Figure S5E), suggesting complementary action by another nutrient. Important with respect to NAD^+/NADH balance, $^{13}C_6$-glucose contributed more to glycerol-3-P, resulting in a further increase in glycerol-3-P levels in pyruvate-deprived AMA-treated cells (Figures 3E and 3F).

These data indicate that extracellular pyruvate is mainly converted to lactate, thereby contributing to NAD^+ regeneration in AMA-treated cells, but it also allows glucose to be converted to alanine and to malate. The results also suggest that AMA-treated SSPCs, but not tumor cells, can metabolically adapt to pyruvate deprivation by increasing the conversion of glucose to glycerol-3-P to maintain their NAD^+/NADH balance.

MDH2 controls NAD^+ regeneration

In many tumor cells, NAD^+ is required for *de novo* aspartate synthesis, as aspartate uptake is limited and aspartate is essential for nucleotide synthesis and, thus, proliferation (Birsoy et al., 2015; Garcia-Bermudez et al., 2018; Sullivan et al., 2015). In contrast, SSPCs consumed extracellular aspartate (Figure S5F) and $^{13}C_4$-aspartate contributed to TCA cycle metabolites malate and fumarate (Figures 3I and S3J) at baseline. AMA treatment increased aspartate uptake and decreased the $^{13}C_4$-aspartate contribution to αKG, but manifestly increased the $^{13}C_4$-aspartate contribution to $^{13}C_4$-succinate (22.6% ± 1.37% versus 1.88% ± 0.08%; AMA versus vehicle; Figures 3I–3K), suggesting that aspartate is not metabolized in the TCA cycle via OAA to citrate but rather to fumarate and finally to succinate by reverse SDH activity.

Given the high contribution of aspartate to TCA cycle metabolites via reverse SDH activity, we hypothesized that aspartate metabolism is important for the NADH/NAD^+ balance and proliferation of AMA-treated SSPCs, especially during pyruvate deprivation, and we therefore performed combined pyruvate and aspartate (Pyr/Asp) deprivation. Of note, depletion of only aspartate did not affect NAD^+ levels or proliferation of SSPCs cultured with or without AMA. In contrast, Pyr/Asp withdrawal decreased NAD^+ levels and BrdU incorporation in AMA-treated SSPCs (Figures 3G and 3H). In comparison, aspartate deprivation of AMA-treated tumor cells did not further decrease the reduced proliferation observed in normal and especially in pyruvate-deprived conditions (Figures S4A–S4H). Thus, extracellular pyruvate is critical for AMA-treated tumor cells but less so for AMA-treated SSPCs, as SSPCs can regenerate electron acceptors by using other nutrients such as aspartate.

The combined Pyr/Asp deprivation resulted in decreased malate levels, suggesting decreased MDH2 activity and, thus, reduced NAD^+ regeneration. This decrease in MDH2 activity is also supported by the reduced 2HG levels (Figure S5G), as MDH2 can convert αKG to 2HG, thereby regenerating NAD^+ (Intlekofer et al., 2017; Ye et al., 2018) (Figure S3J). Pyr/Asp-deprived AMA-treated cells could not compensate for the reduced MDH2 activity by enhancing LDH activity, as lactate levels were not changed, nor by GPDH activity, as glycerol-3-P levels did not additionally increase compared with the pyruvate-deprived condition (Figures S5H and S5I).

To confirm the link between NAD^+ levels and proliferation, we added α-ketobutyrate (AKB), which can be used by intracellular dehydrogenases to regenerate NAD^+ from NADH (Sullivan et al., 2015). Adding AKB to AMA-treated cells, cultured in Pyr/Asp-deprived medium, prevented the decrease in NAD^+ levels and BrdU incorporation (Figures 3L and 3M), indicating that maintaining NAD^+ levels is important to ensure proliferation upon AMA treatment.

Thus, MDH2 activity is important for NAD^+ regeneration and proliferation in AMA-treated cells, by promoting the conversion not only of glucose and aspartate to malate but also of glutamine-derived αKG to 2HG (Figure S3J). To prove this hypothesis, we inactivated *Mdh2* using short hairpin RNA (shRNA) ($Mdh2^{KD}$) (Figures 3N and 3O). However, MDH2 deletion did not affect NAD^+ levels or BrdU incorporation in AMA-treated SSPCs (Figures 3P and 3Q), possibly because the enormous increase in 2HG levels (14-fold) was only reduced by 50% (Figure S5J), thereby allowing sufficient NAD^+ regeneration. Production of 2HG from αKG is indirectly supported by pyruvate uptake in AMA-treated SSPCs (Figures S5B and S5C), as pyruvate promotes the conversion of glucose to alanine and concurrently of glutamate to αKG. We therefore cultured AMA-treated $Mdh2^{KD}$ cells without pyruvate and observed decreased NAD^+ levels and proliferation (Figures 3P and 3Q), indicating that the combination of pyruvate uptake and MDH2 activity is critical to preserve proliferation in AMA-treated SSPCs. Similar to the Pyr/Asp-deprived condition, GPDH activity could not compensate for MDH2 knockdown, as glycerol-3-P levels did not additionally increase compared with the pyruvate-deprived condition, thus explaining the decrease in NAD^+ levels (Figure S5K).

(J) Schematic representation of $^{13}C_4$-aspartate labeling patterns. Empty circles indicate ^{12}C, black circles denote ^{13}C labeling pattern with conversion of oxaloacetate to malate, and gray circles denote ^{13}C labeling pattern with conversion of oxaloacetate to citrate.
(K) M + 2 and M + 4 contribution of $^{13}C_4$-aspartate to suc (n = 4).
(L) NAD^+ levels in cells cultured in full medium or without pyruvate and aspartate (Pyr/Asp), supplemented or not with 1 mM α-ketobutyrate (AKB) (n = 4).
(M) Flow-cytometry analysis of $BrdU^+$ cells treated for 24 h with veh or AMA and cultured in full or no Pyr/Asp medium, supplemented or not with AKB (n = 4).
(N and O) Malate dehydrogenase2 (*Mdh2*) mRNA levels (N, n = 4) and immunoblot detection of MDH2 and β-actin (O) in cells transduced with control ($Mdh2^{CO}$) or *Mdh2*-specific shRNA ($Mdh2^{KD}$). Representative image of three experiments is shown.
(P) NAD^+ levels in veh- and AMA-treated $Mdh2^{CO}$ and $Mdh2^{KD}$ cells cultured with or without pyruvate for 3 days (n = 4).
(Q) Flow-cytometry analysis of $BrdU^+$ $Mdh2^{CO}$ and $Mdh2^{KD}$ cells treated for 24 h with veh or AMA and cultured with or without pyruvate (n = 4).
Data are means ± SD. $^{**}p < 0.01$, $^{***}p < 0.001$, $^{****}p < 0.0001$ versus veh-treated cells (paired two-tailed Student's t test). $^{\$}p < 0.05$ (two-way ANOVA), $^{\S}p < 0.05$ (three-way ANOVA). See also Figures S4–S6.

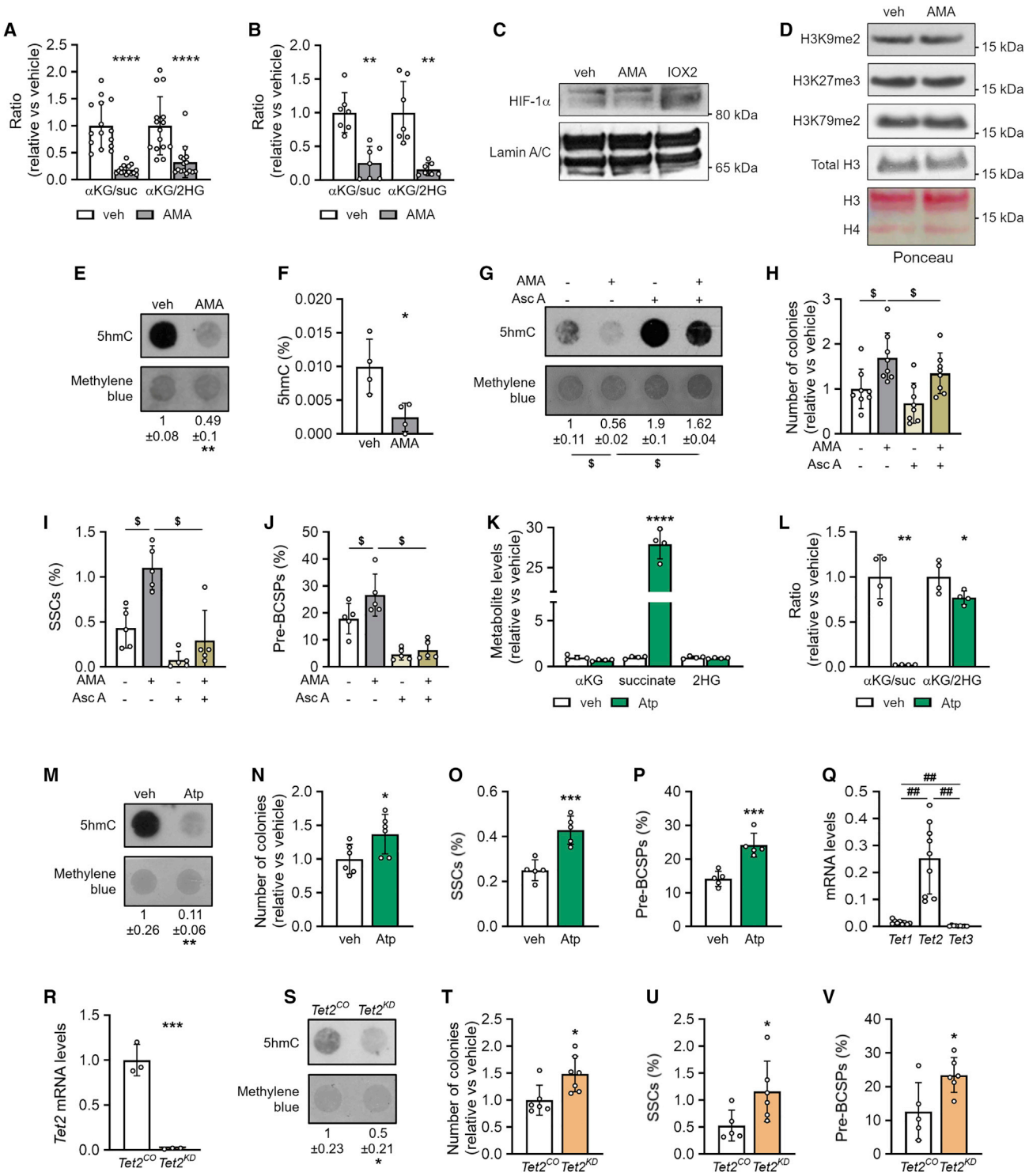

Figure 4. Metabolic changes increase TET activity and preserve SSPCs

(A and B) Ratio of α-ketoglutarate (αKG) to succinate (suc) and of αKG to 2-hydroxyglutarate (2HG) in cells treated with vehicle (veh) or 10 μM AMA for 3 days (A, n = 15) or 3 weeks (B, n = 7).

(C) Immunoblot of HIF-1α with Lamin A/C as loading control in cells treated with veh or AMA for 3 days (n = 3). IOX2, an inhibitor of HIF prolyl hydroxylase 2, was used as positive control. Representative image is shown.

(D) Immunoblot of dimethylated lysine 9 of histone H3 (H3K9me2), trimethylated lysine 27 of histone H3 (H3K27me3), and dimethylated lysine 79 of histone H3 (H3K79me2), with total histone 3 (H3) and Ponceau red as loading control (n = 3). Representative image is shown.

(legend continued on next page)

Overall, metabolism of extracellular pyruvate and MDH2 activity are closely interconnected to enable NAD^+ regeneration and proliferation in SSPCs with ETC dysfunction.

DHODH activity is preserved, allowing pyrimidine synthesis

We next investigated nucleotide synthesis in more detail, given the importance of both NAD^+ and aspartate for this metabolic process. In contrast to several observations in tumor cells (Birsoy et al., 2015; Diehl et al., 2019; Sullivan et al., 2015), the decrease in NAD^+ and proliferation in Pyr/Asp-deprived or Pyr-deprived $Mdh2^{KD}$ AMA-treated SSPCs was not linked to a defect in nucleotide synthesis. Indeed, nucleotide levels were not changed and supplementing nucleotides (Table S1) did not rescue the proliferation defect (Figures S6A–S6C), suggesting that NAD^+ levels regulate proliferation in SSPCs by mechanisms other than nucleotide synthesis. These data indicate that nucleotides can still be synthesized in AMA-treated cells and that DHODH, an enzyme involved in pyrimidine synthesis and indirectly linked to the ETC, is not fully inhibited. DHODH generates orotate from dihydroorotate by transferring electrons to ubiquinone, resulting in the generation of ubiquinol, which is oxidized back to ubiquinone by complex III (Figure S3I). Inhibiting complex III by AMA treatment is thus expected to indirectly block DHODH activity. We observed a decreased orotate/dihydroorotate ratio in AMA-treated cells, indicating that the reaction catalyzed by DHODH was impaired (Figure S6D), but we also noted increased levels of dihydroorotate and orotate, suggesting that DHODH can still produce orotate from dihydroorotate (Figures S6E and S6F). A likely explanation for the preserved, although reduced, DHODH activity is that the reverse SDH activity favors electron transfer from ubiquinol to complex II, allowing ubiquinone to accept electrons from DHODH and pyrimidine synthesis to continue. Indeed, adding atpenin A5 (Atp), an inhibitor of SDH, together with AMA, decreased the contribution of $^{13}C_4$-aspartate to orotate and reduced orotate levels, indicating that DHODH activity depends on SDH activity in AMA-treated cells (Figures S6G and S6H).

Together, these data indicate that skeletal progenitors can maintain their proliferation when complex III is blocked, in part by preserving DHODH activity, likely because of reverse SDH activity.

Metabolic changes increase TET activity and preserve SSPCs

Since AMA-treated SSPCs not only preserved proliferation but also showed improved stemness (Figures 1 and S2), we questioned whether the AMA-induced metabolic changes also supported stemness properties. The metabolic rerouting of the TCA cycle resulted in a significant decrease in the αKG/succinate and αKG/2HG ratios, after both short- and long-term AMA treatment (Figures 4A and 4B), as well as after adding Myx (Figures S7A and S7B).

The accumulation of succinate and 2HG relative to αKG might affect the activity of αKG-dependent dioxygenases, including prolyl hydroxylases that regulate hypoxia-inducible factor α (HIF-α), JmjC domain-containing histone demethylases, and Ten-eleven translocation (TET) DNA demethylases (Intlekofer and Finley, 2019). These enzymes use αKG as co-factor but are inhibited by fumarate, succinate, and 2HG, which all increased in AMA-treated cells. We did not observe changes in HIF-1α levels (Figure 4C) or global histone methylation (Figure 4D). On the other hand, 5-hydroxymethylcytosine (5hmC) levels were reduced in AMA-treated cells (Figures 4E and 4F), suggesting inhibition of TET activity and decreased DNA demethylation. To investigate whether inhibition of TET enzymes was important for SSPC properties, we used three different approaches. First, we treated SSPCs with ascorbic acid, which is known to activate TET enzymes (Blaschke et al., 2013). The addition of ascorbic acid increased 5hmC levels in AMA- and vehicle-treated cells (Figure 4G) and blocked the AMA-induced increase in SSPCs, as evidenced by the reduced number of colonies formed (Figure 4H) and decreased percentage of SSCs and pre-BCSPs (Figures 4I and 4J). Second, we investigated the effect of the SDH inhibitor Atp. Atp treatment increased succinate levels but had no effect on 2HG, and resulted in a decreased αKG/succinate ratio (Figures 4K and 4L), which correlated with a drop in 5hmC levels (Figure 4M). Accordingly, cells expanded with Atp formed more colonies and contained a higher percentage of SSCs and pre-BCSPs (Figures 4N–4P), supporting the link between αKG/succinate ratio, 5hmC levels, and maintenance of SSPCs. Third, to confirm the importance of TET inhibition for SSPC properties, we genetically inactivated *Tet2*, the most expressed DNA demethylase (Figure 4Q). The decreased *Tet2* expression resulted in reduced 5hmC levels (Figures 4R and 4S) and was associated

(E) Dot blot assay of 5-hydroxymethylcytosine (5hmC) in cells treated with veh or AMA for 3 days, with methylene blue staining as loading control. Representative images of four experiments are shown.
(F) Percentage of 5hmC of total cytosine (n = 4).
(G) Dot blot assay of 5hmC in cells treated with veh or AMA in the presence or absence of 0.5 mM ascorbic acid (Asc A) with methylene blue staining as loading control. Representative images of three experiments are shown.
(H–J) Number of colonies formed (H, n = 8), and percentage of SSCs (I, n = 5) and pre-BCSPs (J, n = 5) in cells treated with veh or AMA in the presence or absence of Asc A.
(K and L) αKG, succinate, and 2HG levels (K, n = 4) and ratio of αKG to succinate and of αKG to 2HG (L, n = 4) in cells treated with veh or 500 nM atpenin A5 (Atp).
(M) Dot blot assay of 5hmC in veh- or Atp-treated cells with methylene blue staining as loading control. Representative images of four experiments are shown.
(N–P) Number of colonies formed (N, n = 6), and percentage of SSCs (O, n = 5) and pre-BCSPs (P, n = 5) in cells treated with veh (control) or Atp.
(Q) *Tet1*, *Tet2*, and *Tet3* mRNA levels in periosteal cells (n = 9).
(R) *Tet2* mRNA levels in control ($Tet2^{CO}$) or *Tet2* knockdown ($Tet2^{KD}$) periosteal cells (n = 3).
(S) Dot blot assay of 5hmC in $Tet2^{CO}$ and $Tet2^{KD}$ cells with methylene blue staining as loading control. Representative images of three experiments are shown.
(T–V) Number of colonies formed (T, n = 6–7), and percentage of SSCs (U, n = 5–6) and pre-BCSPs (V, n = 5–6) in $Tet2^{CO}$ and $Tet2^{KD}$ cells.
Data are means ± SD. *p < 0.05, **p < 0.01, ***p < 0.001, ****p < 0.0001 versus veh (two-tailed Student's t test). ##p < 0.01 (one-way ANOVA), $p < 0.05 (two-way ANOVA).

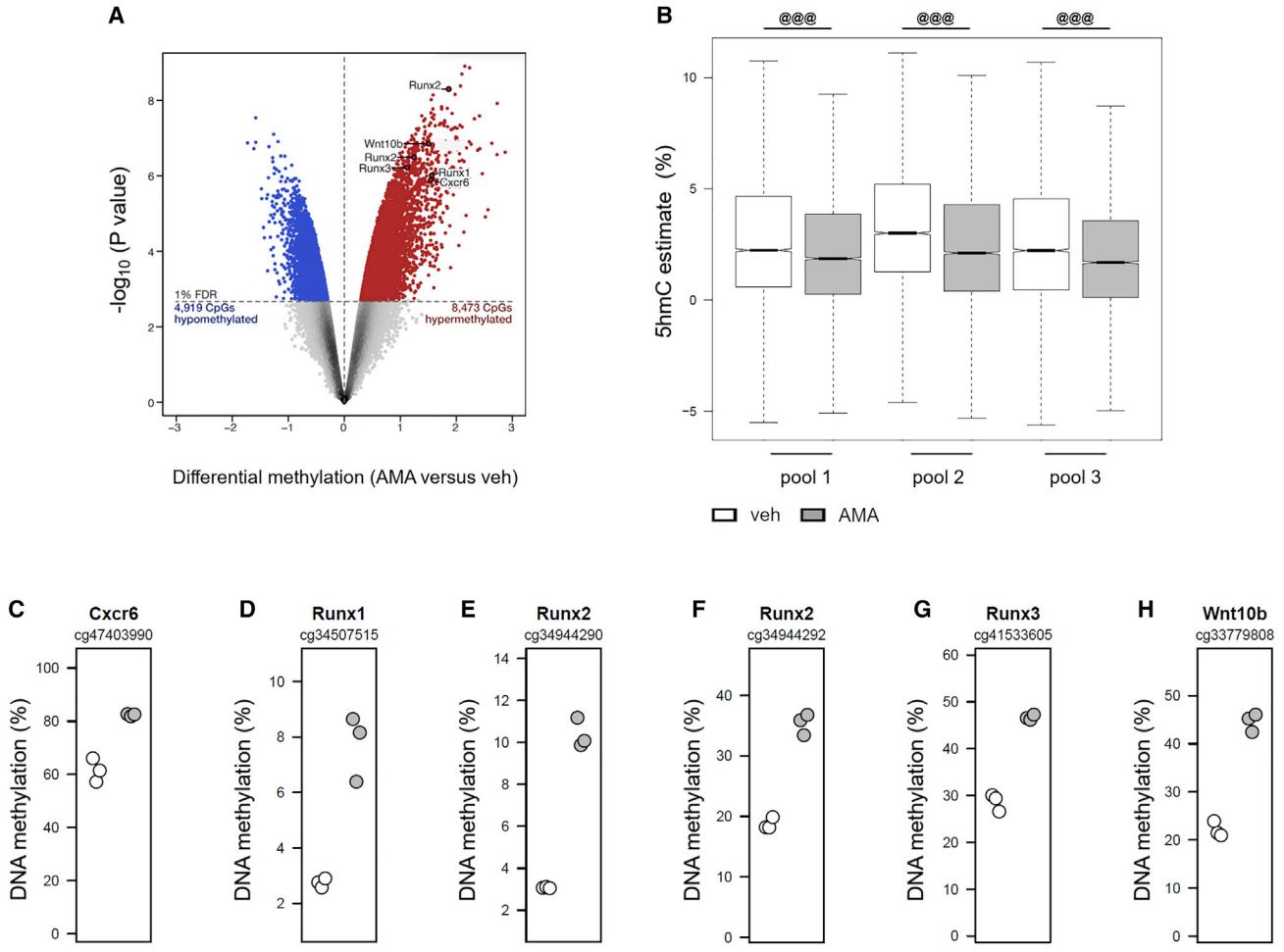

Figure 5. AMA treatment induces DNA hypermethylation

(A) Volcano plot showing differential methylation at CpGs in cells treated with vehicle (veh) or 10 μM AMA for 10 days (n = 3). Probes showing a significant false discovery rate of <1%. DNA hypomethylation and DNA hypermethylation are highlighted in blue and red, respectively. AMA treatment preferentially induced DNA hypermethylation (Fisher's exact test, $p < 10^{-16}$).

(B) 5hmC estimate at CpGs of veh- or AMA-treated cells (n = 3).

(C–H) Examples of AMA-induced DNA hypermethylation at CpGs located in the protein-coding gene promoters of *Cxcr6* (C), *Runx1* (D), *Runx2* (E and F), *Runx3* (G), and *Wnt10b* (H) (n = 3).

Data are means ± SD. $^{@@@}p < 0.001$ (Wilcoxon signed rank test with continuity correction). See also Figure S7.

with an increased capacity to form colonies and a higher percentage of SSCs and pre-BCSPs (Figures 4T–4V).

We next investigated the changes in DNA methylation and demethylation induced by AMA treatment. To this end, DNA was isolated and hybridized to Beadchip microarrays after either bisulfite (BS) conversion to uncover the aggregate levels of 5mC and 5hmC, or after oxidative bisulfite (OxBS) conversion to uncover 5mC levels. Comparison of the OxBS and BS signals revealed that, out of the 282,160 CpGs investigated, 70,325 showed significant levels of 5hmC. The mean estimated 5hmC level at these sites was 2.18% (Figures S7C and S7D), and, as expected, 5hmC was detected mostly at regions with intermediate levels of DNA methylation (Booth et al., 2012). Among these 70,325 CpGs, 8,473 showed DNA hypermethylation and 4,919 showed DNA hypomethylation (1% false discovery rate), indicating that AMA treatment predominantly induces DNA hypermethylation (Figure 5A). Importantly, 5hmC levels were significantly reduced at CpGs showing hypermethylation, suggesting that the observed AMA-induced DNA hypermethylation is due to reduced DNA demethylation activity (Figure 5B). Notably, among the 300 most significantly hypermethylated CpGs, 36 were located in protein-coding gene promoters, including several genes involved in differentiation (*Cxcr6*, *Runx1*, *Runx2*, *Runx3*, and *Wnt10b*; Figures 5C–5H).

AMA-induced metabolic changes thus preserve SSPCs during expansion by inhibiting TET DNA demethylase activity.

MDH2 activity is critical for preserving SSPCs

We hypothesized that the decreased αKG/succinate and αKG/2HG ratios upon AMA treatment were mediated by the observed adaptations in TCA cycle-related glucose, glutamine, and aspartate metabolism (Figures 2I, 2M, and 3I). We focused on MDH2, as this enzyme both converts glucose- and aspartate-derived

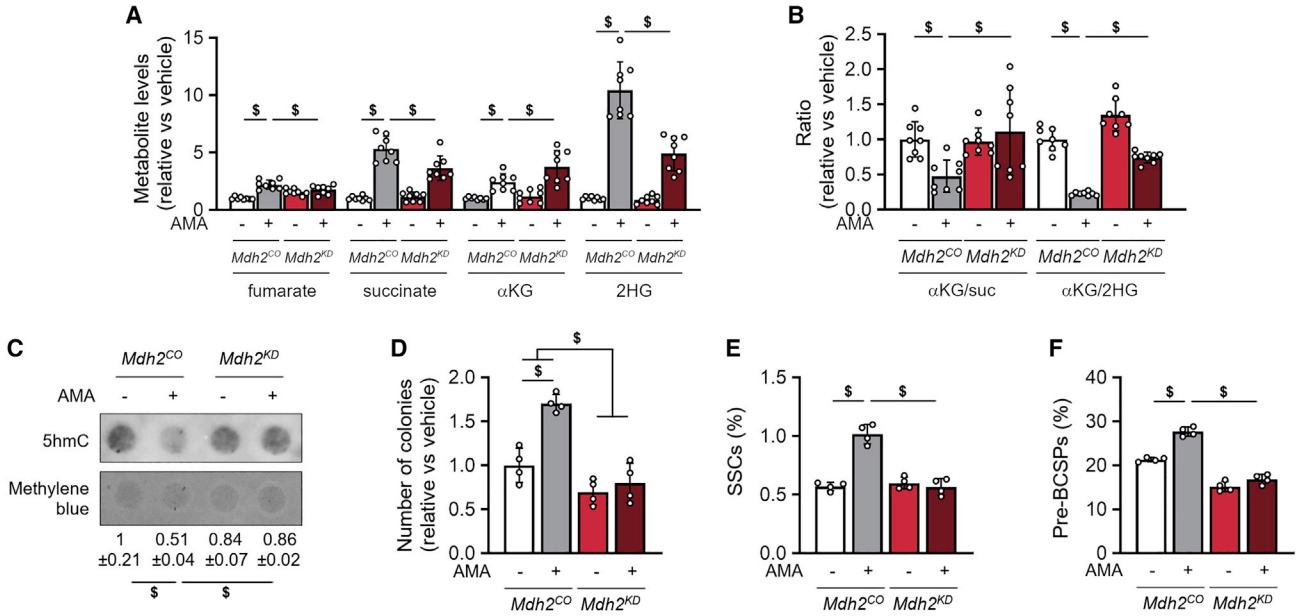

Figure 6. MDH2 activity is critical for preserving SSPCs

(A and B) Fumarate, succinate (suc), α-ketoglutarate (αKG), and 2-hydroxyglutarate (2HG) levels (A, n = 8) and ratios of αKG to suc and of αKG to 2HG (B, n = 8) in cells treated with vehicle (veh) or 10 μM AMA for 3 days and transduced with control (*Mdh2*^{CO}) or *Mdh2*-specific shRNA (*Mdh2*^{KD}).

(C) Dot blot assay of 5hmC in veh- and AMA-treated *Mdh2*^{CO} and *Mdh2*^{KD} cells with methylene blue staining as loading control. Representative images of four experiments are shown.

(D–F) Number of colonies formed (D, n = 4), and percentage of SSCs (E, n = 4) and pre-BCSPs (F, n = 4) in veh- and AMA-treated *Mdh2*^{CO} and *Mdh2*^{KD} cells. Data are means ± SD. $^{\$}p < 0.05$ (two-way ANOVA).

OAA to malate, which is then metabolized to succinate by reverse SDH activity, and also converts glutamine-derived αKG to 2HG, and hence contributes to the increase in succinate and 2HG (Figure S3J). Accordingly, MDH2 inactivation suppressed the AMA-induced increase in fumarate, succinate, and 2HG levels, while it further enhanced αKG levels (Figure 6A), thereby normalizing αKG/succinate and αKG/2HG ratios (Figure 6B). In addition, MDH2 inactivation prevented the AMA-induced decrease in 5hmC levels and inhibited the increase in colony formation and percentage of SSCs and pre-BCSPs (Figures 6C–6F).

Thus, AMA treatment of SSPCs decreases αKG/2HG and αKG/succinate ratios by a dual mechanism: first, by enhancing the conversion of glutamine to 2HG via MDH2 and second, by increasing the conversion of glucose and especially aspartate to malate via MDH2 and further to succinate via reverse SDH activity (Figure S7E). These metabolic changes inhibit TET activity, resulting in maintenance of SSPC properties.

Periosteal cells expanded with AMA form more bone *in vivo*

To validate that the preserved self-renewal and SSPC properties are physiologically relevant, we investigated whether AMA-treated cells showed increased bone formation after *in vivo* implantation. To this end, we used an ectopic model of direct bone formation in mice (Stegen et al., 2016). Histomorphometry showed that, 8 weeks after implantation, scaffolds seeded with AMA-treated mPDCs contained significantly more bone compared with the vehicle-treated condition (Figures 7A and 7B). To distinguish the implanted from the host-derived cells, we used mPDCs isolated from C57BL/6-ACTb-eGFP mice and found that in both AMA-treated and control conditions the new bone was formed by the implanted cells, as cells positive for the osteogenic marker Osterix co-expressed GFP (Figures 7C and 7D).

The increased bone mass in implants containing AMA-treated mPDCs was not caused by increased survival of the implanted cells (Figure 7E) or enhanced vascularization (Figures 7F–7H). Instead, we observed a higher number of SSPCs in the AMA-treated condition, based on the following observation. Prior to implantation, donor cells were labeled with CellTracker CMFDA, and the surviving implanted cells (CMFDA^{+}/PI^{-}) were retrieved from the scaffold 3 days after implantation and seeded for colony formation. Again, the AMA-treated cells formed more colonies compared with controls (Figures 7I and 7J), indicating that this cell population continues to contain more SSPCs after *in vivo* implantation.

In conclusion, AMA treatment during expansion of SSPCs preserves their self-renewal and bone-forming capacity, resulting in better *in vivo* bone formation.

DISCUSSION

In this study, we show that the metabolic plasticity of mouse SSPCs promotes their proliferation and self-renewal in response to ETC complex III inhibition. Mechanistically, several NAD^{+} regenerating pathways were induced to preserve proliferation,

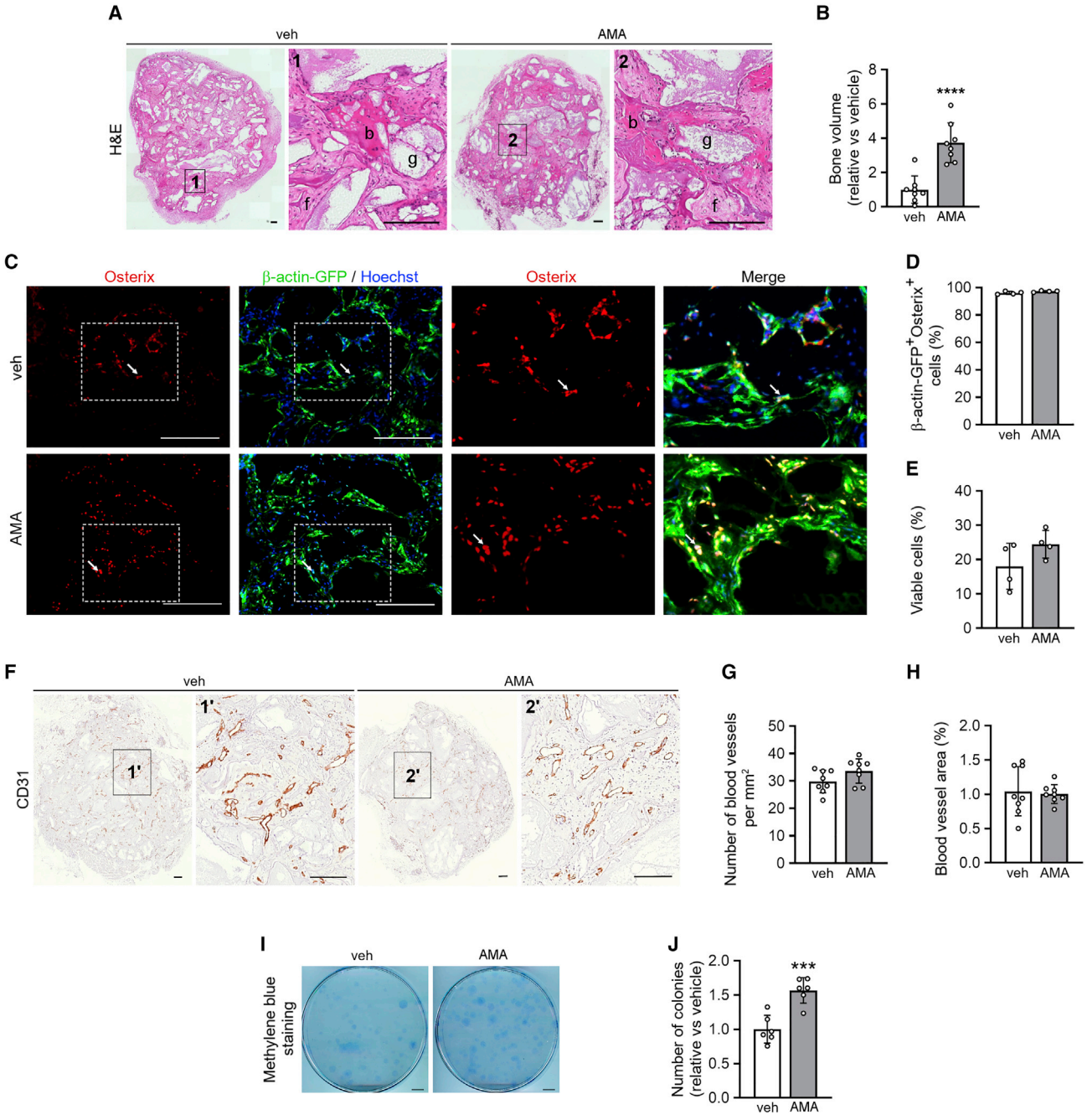

Figure 7. Periosteal cells expanded with AMA form more bone *in vivo*

(A) H&E staining of ectopic implants, seeded with mPDCs treated with vehicle (veh) or 10 μM AMA for 3 weeks and implanted for 8 weeks (right panel is magnification of boxed area). b, bone; f, fibrous tissue; g, scaffold granule (n = 8).

(B) Quantification of the bone volume formed (n = 8).

(C and D) Osterix and Hoechst (DNA) staining of ectopic implants seeded with β-actin-GFP$^+$ periosteal cells and implanted for 8 weeks (C, n = 4) with quantification of the percentage of β-actin-GFP$^+$ cells within the Osterix$^+$ population (D, n = 4). Magnifications of the boxed area show Osterix staining or merged pictures; white arrows point at β-actin-GFP$^+$/Osterix$^+$ cells.

(E) Viability of mPDCs, labeled prior to implantation with CellTracker Green CMFDA. Viability of CMFDA$^+$ cells was determined after implantation for 3 days by annexin V-propidium iodide flow cytometry (n = 4).

(F–H) CD31 staining of ectopic implants, seeded with mPDCs and implanted for 8 weeks (F; right panel is magnification of boxed area; scale bars, 200 μm; n = 8), with quantification of the number of blood vessels per mm^2 (G) and blood vessel surface area (H) (n = 8).

(legend continued on next page)

comprising changes in glycolysis side pathways that were highly interconnected with rerouting of the TCA cycle. MDH2 and reverse SDH activity proved essential not only for NAD^+ regeneration that supported proliferation but also for the increased 2HG and succinate levels causing epigenetic changes by inhibiting TET DNA demethylase activity resulting in SSPC maintenance. These findings highlight the metabolic flexibility of stem cells and may aid in the development of metabolic strategies that prevent exhaustion of stem cells during *in vitro* expansion and improve cell-based regeneration.

Blocking ETC did not decrease the proliferation of SSPCs, whereas it reduced proliferation in the tested tumor cells, when cultured with identical levels of pyruvate and aspartate. SSPCs were able to preserve their NADH/NAD^+ balance through combined adaptations in several metabolic pathways: NAD^+ was regenerated by increased conversion of glucose to glycerol-3-P, less NADH was produced in the rerouted TCA cycle and, importantly, SDH activity was reversed, which enabled the transfer of electrons from complex I to ubiquinone and regeneration of NAD^+. By reversing SDH activity, aspartate- or glucose-derived fumarate functions as a final electron acceptor in the ETC. MDH2 activity was important to maintain proliferation and regenerate NAD^+ by converting aspartate- and glucose-derived OAA to malate and glutamine-derived αKG to 2HG, reactions that were favored by, but not dependent on, pyruvate uptake. Tumor cells, on the other hand, rely more on the uptake of pyruvate, which contributes to the synthesis of aspartate that is required for nucleotide synthesis, as aspartate uptake is often very limited in tumor cells (Birsoy et al., 2015; Diehl et al., 2019; Sullivan et al., 2015). The highly intertwined and rearranged metabolism of four major nutrients—glucose, glutamine, aspartate, and pyruvate—likely explains the ability of SSPCs to preserve proliferation when encountering ETC shutdown.

The response of SSPCs to ETC inhibition differs from tumor cells in a second aspect, as the correlation between NAD^+ levels and proliferation cannot be explained by nucleotide levels, an observation that was also reported in hematopoietic stem cells (Anso et al., 2017). Further investigation is needed to understand how NAD^+ levels ensure proliferation of AMA-treated SSPCs, but a possible mechanism is that NAD^+ exerts its proliferation-supporting effect via sirtuin-dependent pathways, which modulate gene transcription and energy metabolism (Anderson et al., 2017).

The normal nucleotide levels in AMA-treated SSPCs can be explained by the reverse SDH activity, which converts glucose- and aspartate-derived fumarate to succinate and leads to a rearranged electron transfer. This reverse SDH activity might favor electron transfer from ubiquinol to complex II thereby regenerating ubiquinone, which then can accept electrons from DHODH and thus allows pyrimidine synthesis (Figure S3J). Until recently, reverse SDH has been poorly described and reported to be active during heart ischemia and in the hypoxic environment of the retina (Bisbach et al., 2020; Chouchani et al., 2014). A recent study, published during the review process of our manuscript, revealed that reverse SDH activity may be more common than expected, with tissues such as liver and kidney using fumarate as terminal electron acceptor independent of oxygen levels (Spinelli et al., 2021). The exact cell types, besides SSPCs, that are capable of activating this mechanism remain to be determined, as well as the conditions under which reverse SDH activity can occur.

ETC inhibition in SSPCs prevented their exhaustion, and we discovered that the combination of MDH2 and reverse SDH activity is the major driver of the metabolic adaptations. The increased 2HG and succinate levels, relative to αKG, induce the epigenetic changes that maintain stem cell properties. Whether a similar metabolic rewiring explains the connection between complex III and stemness observed in hematopoietic stem cells (Anso et al., 2017) needs additional exploration. Since preserved proliferation and stem cell properties in AMA-treated SSPCs are explained by the same metabolic adaptations, an appealing hypothesis is that the increased NADH levels are causing the metabolic reprogramming necessary not only to preserve proliferation but also to maintain stem cell properties. This concept on the driver function of NADH further expands on recent findings showing that it is the requirement for NAD^+/NADH homeostasis rather than the demand for ATP that drives cells to switch to glycolysis (Luengo et al., 2020).

Altogether, our study shows that targeting skeletal progenitor metabolism is beneficial to control self-renewal and cell fate during expansion. Maintaining these *in vitro* properties is of interest to improve cell-based regenerative strategies, as evidenced by the increased bone formation observed when implanting AMA-treated cells *in vivo*. Preserving stem and progenitor properties by interfering with cellular metabolism is thus a promising approach, not only for bone regeneration but likely also for regenerative medicine in general. In addition, the described metabolic plasticity of SSPCs might reflect their capability to cope with changing conditions in the environment. Indeed, following fracture, skeletal progenitors in the periosteum start to proliferate despite the emerging local hypoxia. In normoxia, oxygen is considered a terminal electron acceptor, allowing electron flow through the ETC to persist, which is critical not only for energetics but also for biosynthetic processes. Based on our data, we speculate that hypoxic SSPCs might use fumarate as electron acceptor instead of oxygen by reversing SDH, thereby not only preventing reductive stress but also permitting nucleotide synthesis. In addition, hypoxia has been reported to increase 2HG levels and to inhibit TET activity (Intlekofer et al., 2015; Oldham et al., 2015; Thienpont et al., 2016). Taking our findings together, we propose that SSPCs have the metabolic flexibility to adapt to a hypoxic environment without loss of proliferation and SSPC properties and thereby support efficient fracture repair, although further research is needed.

Limitations of the study

This study has some limitations, as the metabolic plasticity of SSPC needs to be confirmed in human skeletal progenitors. In addition, it would be interesting to investigate which microenvironments in the skeleton favor these metabolic adaptations

(I and J) Visualization (I, methylene blue staining) and quantification of colonies formed by $CMFDA^+/PI^-$ cells isolated 3 days after implantation and cultured for 1 week (J, n = 6).

Data are means ± SD. ***p < 0.001, ****p < 0.0001 versus veh (unpaired two-tailed Student's t test). Scale bars, 200 μm (A, C) and 1 cm (I).

and thereby allow proliferation and self-renewal of SSPCs. Further mechanistic studies are required to understand how NAD^+ levels affect SSPC proliferation, if not by changing nucleotide synthesis, and whether all of the identified NAD^+ regenerating pathways are equally important for the phenotype.

STAR★METHODS

Detailed methods are provided in the online version of this paper and include the following:

- KEY RESOURCES TABLE
- RESOURCE AVAILABILITY
  - Lead contact
  - Materials availability
  - Data and code availability
- EXPERIMENTAL MODEL AND SUBJECT DETAILS
  - Animals
  - Cell lines
  - Primary cell culture
- METHOD DETAILS
  - Cell culture
  - Genetic targeting
  - Flow cytometry analysis and cell sorting
  - RNA extraction and quantitative real-time (qRT)-PCR
  - Western blot
  - DNA methylation/hydroxymethylation analysis
  - Metabolic analyses
  - Mouse model of bone regeneration
  - (Immuno)histochemistry
- QUANTIFICATION AND STATISTICAL ANALYSIS

SUPPLEMENTAL INFORMATION

Supplemental information can be found online at https://doi.org/10.1016/j.celrep.2022.111105.

ACKNOWLEDGMENTS

We wish to thank Ingrid Stockmans for technical assistance. G.C. acknowledges funding from Fund for Scientific Research – Flanders (FWO: G.0A42.16 and G.0B3418) and from KU Leuven (C24/17/077). S.L. is a doctoral fellow from the FWO (1S46318N). S.S. is a postdoctoral fellow from the FWO (12H5917N). G.R. has received consecutive PhD fellowships from Kom op tegen Kanker and FWO (1137117N and 1137119N). The Hercules Fund of the FWO is acknowledged for their financial support of the project I013518N. S.-M.F. acknowledges funding from the European Research Council under the ERC Consolidator Grant Agreement no. 771486 – MetaRegulation, FWO – Research Projects (G098120N, G088318N), KU Leuven – FTBO, and Fonds Baillet Latour. Schematics included in the figures were created using BioRender.com and Servier Medical Art templates.

AUTHOR CONTRIBUTIONS

G.T., N.v.G., and G.C. conceptualized and designed the study. G.T., S.L., and S.T. performed the *in vitro* experiments. G.T. and S.S. performed the *in vivo* experiments. K.M. performed histology. G.T., G.R., G.E., P.C., S.-M.F., B.T., and B.G. contributed to the design, execution, and interpretation of the metabolic or epigenetic experiments. G.T. and G.C. interpreted the data and wrote the manuscript. G.C. supervised the study.

DECLARATION OF INTERESTS

The authors declare no competing interests.

Received: September 7, 2021
Revised: April 13, 2022
Accepted: June 25, 2022
Published: July 26, 2022

REFERENCES

Anderson, K.A., Madsen, A.S., Olsen, C.A., and Hirschey, M.D. (2017). Metabolic control by sirtuins and other enzymes that sense NAD(+), NADH, or their ratio. Biochim. Biophys. Acta Bioenerg. *1858*, 991–998. https://doi.org/10.1016/j.bbabio.2017.09.005.

Ansó, E., Weinberg, S.E., Diebold, L.P., Thompson, B.J., Malinge, S., Schumacker, P., Liu, X., Zhang, Y., Shao, Z., Steadman, M., et al. (2017). The mitochondrial respiratory chain is essential for haematopoietic stem cell function. Nat. Cell Biol. *19*, 614–625. https://doi.org/10.1038/ncb3529.

Bao, X.R., Ong, S.E., Goldberger, O., Peng, J., Sharma, R., Thompson, D.A., Vafai, S.B., Cox, A.G., Marutani, E., Ichinose, F., et al. (2016). Mitochondrial dysfunction remodels one-carbon metabolism in human cells. Elife *5*, e10575. https://doi.org/10.7554/eLife.10575.

Bianco, P., Cao, X., Frenette, P.S., Mao, J.J., Robey, P.G., Simmons, P.J., and Wang, C.Y. (2013). The meaning, the sense and the significance: translating the science of mesenchymal stem cells into medicine. Nat. Med. *19*, 35–42. https://doi.org/10.1038/nm.3028.

Birsoy, K., Wang, T., Chen, W., Freinkman, E., Abu-Remaileh, M., and Sabatini, D. (2015). An essential role of the mitochondrial electron transport chain in cell proliferation is to enable aspartate synthesis. Cell *162*, 540–551. https://doi.org/10.1016/j.cell.2015.07.016.

Bisbach, C.M., Hass, D.T., Robbings, B.M., Rountree, A.M., Sadilek, M., Sweet, I.R., and Hurley, J.B. (2020). Succinate can shuttle reducing power from the hypoxic retina to the O2-rich pigment epithelium. Cell Rep. *31*, 107606. https://doi.org/10.1016/j.celrep.2020.107606.

Blaschke, K., Ebata, K.T., Karimi, M.M., Zepeda-Martínez, J.A., Goyal, P., Mahapatra, S., Tam, A., Laird, D.J., Hirst, M., Rao, A., et al. (2013). Vitamin C induces Tet-dependent DNA demethylation and a blastocyst-like state in ES cells. Nature *500*, 222–226. https://doi.org/10.1038/nature12362.

Booth, M.J., Branco, M.R., Ficz, G., Oxley, D., Krueger, F., Reik, W., and Balasubramanian, S. (2012). Quantitative sequencing of 5-methylcytosine and 5-hydroxymethylcytosine at single-base resolution. Science *336*, 934–937. https://doi.org/10.1126/science.1220671.

Buescher, J.M., Antoniewicz, M.R., Boros, L.G., Burgess, S.C., Brunengraber, H., Clish, C.B., DeBerardinis, R.J., Feron, O., Frezza, C., Ghesquiere, B., et al. (2015). A roadmap for interpreting (13)C metabolite labeling patterns from cells. Curr. Opin. Biotechnol. *34*, 189–201. https://doi.org/10.1016/j.copbio.2015.02.003.

Chan, C., Seo, E., Chen, J., Lo, D., McArdle, A., Sinha, R., Tevlin, R., Seita, J., Vincent-Tompkins, J., Wearda, T., et al. (2015). Identification and specification of the mouse skeletal stem cell. Cell *160*, 285–298. https://doi.org/10.1016/j.cell.2014.12.002.

Chouchani, E.T., Pell, V.R., Gaude, E., Aksentijević, D., Sundier, S.Y., Robb, E.L., Logan, A., Nadtochiy, S.M., Ord, E.N.J., Smith, A.C., et al. (2014). Ischaemic accumulation of succinate controls reperfusion injury through mitochondrial ROS. Nature *515*, 431–435. https://doi.org/10.1038/nature13909.

Colnot, C. (2009). Skeletal cell fate decisions within periosteum and bone marrow during bone regeneration. J. Bone Miner. Res. *24*, 274–282. https://doi.org/10.1359/jbmr.081003.

De Borre, M., and Branco, M.R. (2021). Oxidative bisulfite sequencing: an experimental and computational protocol. Methods Mol. Biol. *2198*, 333–348. https://doi.org/10.1007/978-1-0716-0876-0_26.

Diebold, L.P., Gil, H.J., Gao, P., Martinez, C.A., Weinberg, S.E., and Chandel, N.S. (2019). Mitochondrial complex III is necessary for endothelial cell

proliferation during angiogenesis. Nat. Metab. *1*, 158–171. https://doi.org/10.1038/s42255-018-0011-x.

Diehl, F.F., Lewis, C.A., Fiske, B.P., and Vander Heiden, M.G. (2019). Cellular redox state constrains serine synthesis and nucleotide production to impact cell proliferation. Nat. Metab. *1*, 861–867. https://doi.org/10.1038/s42255-019-0108-x.

Fendt, S.M., Bell, E.L., Keibler, M.A., Olenchock, B.A., Mayers, J.R., Wasylenko, T.M., Vokes, N.I., Guarente, L., Heiden, M.G.V., and Stephanopoulos, G. (2013). Reductive glutamine metabolism is a function of the alpha-ketoglutarate to citrate ratio in cells. Nat. Commun. *4*, 2236. https://doi.org/10.1038/ncomms3236.

Garcia-Bermudez, J., Baudrier, L., La, K., Zhu, X.G., Fidelin, J., Sviderskiy, V.O., Papagiannakopoulos, T., Molina, H., Snuderl, M., Lewis, C.A., et al. (2018). Aspartate is a limiting metabolite for cancer cell proliferation under hypoxia and in tumours. Nat. Cell Biol. *20*, 775–781. https://doi.org/10.1038/s41556-018-0118-z.

Gui, D., Sullivan, L., Luengo, A., Hosios, A., Bush, L., Gitego, N., Davidson, S., Freinkman, E., Thomas, C., and Vander Heiden, M. (2016). Environment dictates dependence on mitochondrial complex I for NAD+ and aspartate production and determines cancer cell sensitivity to metformin. Cell Metab. *24*, 716–727. https://doi.org/10.1016/j.cmet.2016.09.006.

Intlekofer, A., Dematteo, R., Venneti, S., Finley, L., Lu, C., Judkins, A., Rustenburg, A., Grinaway, P., Chodera, J., Cross, J., and Thompson, C. (2015). Hypoxia induces production of L-2-hydroxyglutarate. Cell Metab. *22*, 304–311. https://doi.org/10.1016/j.cmet.2015.06.023.

Intlekofer, A.M., and Finley, L.W.S. (2019). Metabolic signatures of cancer cells and stem cells. Nat. Metab. *1*, 177–188. https://doi.org/10.1038/s42255-019-0032-0.

Intlekofer, A.M., Wang, B., Liu, H., Shah, H., Carmona-Fontaine, C., Rustenburg, A.S., Salah, S., Gunner, M.R., Chodera, J.D., Cross, J.R., and Thompson, C.B. (2017). L-2-Hydroxyglutarate production arises from noncanonical enzyme function at acidic pH. Nat. Chem. Biol. *13*, 494–500. https://doi.org/10.1038/nchembio.2307.

Kennedy, B.E., Sharif, T., Martell, E., Dai, C., Kim, Y., Lee, P.W., and Gujar, S.A. (2016). NAD(+) salvage pathway in cancer metabolism and therapy. Pharmacol. Res. *114*, 274–283. https://doi.org/10.1016/j.phrs.2016.10.027.

Liu, S., Fu, S., Wang, G., Cao, Y., Li, L., Li, X., Yang, J., Li, N., Shan, Y., Cao, Y., et al. (2021). Glycerol-3-phosphate biosynthesis regenerates cytosolic NAD(+) to alleviate mitochondrial disease. Cell Metab. *33*, 1974–1987.e9. https://doi.org/10.1016/j.cmet.2021.06.013.

Luengo, A., Li, Z., Gui, D.Y., Sullivan, L.B., Zagorulya, M., Do, B.T., Ferreira, R., Naamati, A., Ali, A., Lewis, C.A., et al. (2020). Increased demand for NAD(+) relative to ATP drives aerobic glycolysis. Mol. Cell *81*, 691–707.e6. https://doi.org/10.1016/j.molcel.2020.12.012.

Lunt, S.Y., and Vander Heiden, M.G. (2011). Aerobic glycolysis: meeting the metabolic requirements of cell proliferation. Annu. Rev. Cell Dev. Biol. *27*, 441–464. https://doi.org/10.1146/annurev-cellbio-092910-154237.

Moran-Crusio, K., Reavie, L., Shih, A., Abdel-Wahab, O., Ndiaye-Lobry, D., Lobry, C., Figueroa, M., Vasanthakumar, A., Patel, J., Zhao, X., et al. (2011). Tet2 loss leads to increased hematopoietic stem cell self-renewal and myeloid transformation. Cancer Cell *20*, 11–24. https://doi.org/10.1016/j.ccr.2011.06.001.

Oldham, W., Clish, C., Yang, Y., and Loscalzo, J. (2015). Hypoxia-mediated increases in L-2-hydroxyglutarate coordinate the metabolic response to reductive stress. Cell Metab. *22*, 291–303. https://doi.org/10.1016/j.cmet.2015.06.021.

Pereira, S.L., Grãos, M., Rodrigues, A.S., Anjo, S.I., Carvalho, R.A., Oliveira, P.J., Arenas, E., and Ramalho-Santos, J. (2013). Inhibition of mitochondrial complex III blocks neuronal differentiation and maintains embryonic stem cell pluripotency. PLoS One *8*, e82095. https://doi.org/10.1371/journal.pone.0082095.

Sacchetti, B., Funari, A., Michienzi, S., Di Cesare, S., Piersanti, S., Saggio, I., Tagliafico, E., Ferrari, S., Robey, P.G., Riminucci, M., and Bianco, P. (2007). Self-renewing osteoprogenitors in bone marrow sinusoids can organize a hematopoietic microenvironment. Cell *131*, 324–336. https://doi.org/10.1016/j.cell.2007.08.025.

Spinelli, J.B., Rosen, P.C., Sprenger, H.G., Puszynska, A.M., Mann, J.L., Roessler, J.M., Cangelosi, A.L., Henne, A., Condon, K.J., Zhang, T., et al. (2021). Fumarate is a terminal electron acceptor in the mammalian electron transport chain. Science *374*, 1227–1237. https://doi.org/10.1126/science.abi7495.

Stegen, S., Laperre, K., Eelen, G., Rinaldi, G., Fraisl, P., Torrekens, S., Van Looveren, R., Loopmans, S., Bultynck, G., Vinckier, S., et al. (2019). HIF-1α metabolically controls collagen synthesis and modification in chondrocytes. Nature *565*, 511–515. https://doi.org/10.1038/s41586-019-0874-3.

Stegen, S., van Gastel, N., Eelen, G., Ghesquière, B., D'Anna, F., Thienpont, B., Goveia, J., Torrekens, S., Van Looveren, R., Luyten, F., et al. (2016). HIF-1α promotes glutamine-mediated redox homeostasis and glycogen-dependent bioenergetics to support postimplantation bone cell survival. Cell Metab. *23*, 265–279. https://doi.org/10.1016/j.cmet.2016.01.002.

Stiers, P., Stegen, S., van Gastel, N., Van Looveren, R., Torrekens, S., and Carmeliet, G. (2019). Inhibition of the oxygen sensor PHD2 enhances tissue-engineered endochondral bone formation. J. Bone Miner. Res. *34*, 333–348. https://doi.org/10.1002/jbmr.3599.

Sullivan, L., Gui, D., Hosios, A., Bush, L., Freinkman, E., and Vander Heiden, M. (2015). Supporting aspartate biosynthesis is an essential function of respiration in proliferating cells. Cell *162*, 552–563. https://doi.org/10.1016/j.cell.2015.07.017.

Thapa, M., and Dallmann, G. (2020). Role of coenzymes in cancer metabolism. Semin. Cell Dev. Biol. *98*, 44–53. https://doi.org/10.1016/j.semcdb.2019.05.027.

Thienpont, B., Steinbacher, J., Zhao, H., D'Anna, F., Kuchnio, A., Ploumakis, A., Ghesquière, B., Van Dyck, L., Boeckx, B., Schoonjans, L., et al. (2016). Tumour hypoxia causes DNA hypermethylation by reducing TET activity. Nature *537*, 63–68. https://doi.org/10.1038/nature19081.

Tournaire, G., Stegen, S., Giacomini, G., Stockmans, I., Moermans, K., Carmeliet, G., and van Gastel, N. (2020). Nestin-GFP transgene labels skeletal progenitors in the periosteum. Bone *133*, 115259. https://doi.org/10.1016/j.bone.2020.115259.

van Gastel, N., Stegen, S., Eelen, G., Schoors, S., Carlier, A., Daniëls, V.W., Baryawno, N., Przybylski, D., Depypere, M., Stiers, P.J., et al. (2020). Lipid availability determines fate of skeletal progenitor cells via SOX9. Nature *579*, 111–117. https://doi.org/10.1038/s41586-020-2050-1.

van Gastel, N., Torrekens, S., Roberts, S.J., Moermans, K., Schrooten, J., Carmeliet, P., Luttun, A., Luyten, F.P., and Carmeliet, G. (2012). Engineering vascularized bone: osteogenic and proangiogenic potential of murine periosteal cells. Stem Cell *30*, 2460–2471. https://doi.org/10.1002/stem.1210.

Varum, S., Momčilović, O., Castro, C., Ben-Yehudah, A., Ramalho-Santos, J., and Navara, C.S. (2009). Enhancement of human embryonic stem cell pluripotency through inhibition of the mitochondrial respiratory chain. Stem Cell Res. *3*, 142–156. https://doi.org/10.1016/j.scr.2009.07.002.

Vasan, K., Werner, M., and Chandel, N.S. (2020). Mitochondrial metabolism as a target for cancer therapy. Cell Metab. *32*, 341–352. https://doi.org/10.1016/j.cmet.2020.06.019.

Ye, D., Guan, K.L., and Xiong, Y. (2018). Metabolism, activity, and targeting of D- and L-2-hydroxyglutarates. Trends Cancer *4*, 151–165. https://doi.org/10.1016/j.trecan.2017.12.005.

Zhang, X., Xie, C., Lin, A.S., Ito, H., Awad, H., Lieberman, J.R., Rubery, P.T., Schwarz, E.M., O'Keefe, R.J., and Guldberg, R.E. (2005). Periosteal progenitor cell fate in segmental cortical bone graft transplantations: implications for functional tissue engineering. J. Bone Miner. Res. *20*, 2124–2137. https://doi.org/10.1359/JBMR.050806.

STAR★METHODS

KEY RESOURCES TABLE

REAGENT or RESOURCE	SOURCE	IDENTIFIER
Antibodies		
Rabbit polyclonal anti-AMPKα	Cell Signaling Technology	Cat# 2532, RRID:AB_330331
Rabbit monoclonal anti-phospho-AMPKα (Thr172)	Cell Signaling Technology	Cat# 2535 (40H9), RRID:AB_331250
Mouse monoclonal anti-β-actin	Sigma-Aldrich	Cat# A5441 (AC-15), RRID:AB_476744
Rabbit polyclonal anti-HIF1α	Novus Biologicals	Cat# NB100-449, RRID:AB_10001045
Rabbit monoclonal anti-histone H3	Cell Signaling Technology	Cat# 4499 (D1H2), RRID:AB_10544537
Rabbit monoclonal anti-dimethyl-histone H3 (Lys9)	Abcam	Cat# ab176882, RRID:AB_2895140
Rabbit monoclonal anti-trimethyl H3 (Lys27)	Abcam	Cat# ab192985, RRID:AB_2650559
Rabbit polyclonal anti-dimethyl histone H3 (K79)	Abcam	Cat# ab3594, RRID:AB_91530
Rabbit polyclonal anti-5-hydroxymethylcytosine	Active Motif	Cat# 39769, RRID:AB_10013602
Goat polyclonal anti-Lamin A/C	Santa Cruz	Cat# sc-6215, RRID:AB_648152
Rabbit polyclonal anti-MDH2	Abcam	Cat# ab96193, RRID:AB_10679348
Rabbit polyclonal anti-PC	Invitrogen	Cat# PA5-50101, RRID:AB_2635554
Rat monoclonal anti-CD31 (PECAM-1), APC	eBioscience	Cat# 17-0311-80, RRID:AB_657736
Rat anti-mouse CD31	BD Pharmingen	Cat# 550274, RRID:AB_393571
Rat monoclonal anti-CD45, APC	eBioscience	Cat# 17-0451-83, RRID:AB_469393
Rat monoclonal anti-CD51 (Integrin alpha V), Biotin	eBioscience	Cat# 13-0512-82, RRID:AB_466477
Rat monoclonal anti-CD90.2 (Thy-1.2), PE	eBioscience	Cat# 12-0903-81, RRID:AB_465778
Rat monoclonal anti-CD105 (Endoglin), PE	eBioscience	Cat# 12-1051-81, RRID:AB_657526
Rat monoclonal anti-CD200, PerCP-eFluor 710	eBioscience	Cat# 46-5200-82, RRID:AB_10598213
Rat monoclonal anti-CD249 (BP-1), PE	eBioscience	Cat# 12-5891-81, RRID:AB_466014
Rabbit polyclonal anti-GFP	Invitrogen	Cat# A11122, RRID:AB_2307355
Rabbit polyclonal anti-OSX	Santa Cruz	Cat# SC-22536-R, RRID:AB_831618
Rabbit polyclonal anti-mouse-HRP	Dako	Cat# P0161, RRID:AB_2687969
Rabbit polyclonal anti-goat-HRP	Dako	Cat# P0160, RRID:AB_2617143
Goat polyclonal anti-rabbit-Alexa 546	Invitrogen	Cat# A11010, RRID:AB_2534077
Goat polyclonal anti-rabbit-alexa 488	Invitrogen	Cat# A11008, RRID:AB_143165
Goat polyclonal anti-rabbit-HRP	Dako	Cat# P0448, RRID:AB_2617138
Goat polyclonal anti-rat-Biot	BD Pharmingen	Cat# 559286, RRID:AB_397214
Streptavidin PE-Cyanine7 Conjugate	eBioscience	Cat# 25-4317-82, RRID:AB_10116480
Rat monoclonal anti-TER-119, APC	eBioscience	Cat# 17-5921-83, RRID:AB_469474
Chemicals, peptides, and recombinant proteins		
$^{13}C_6$-glucose	Cambridge Isotope Laboratories	Cat# CLM-1396
$^{13}C_5$-glutamine	Cambridge Isotope Laboratories	Cat# CLM-1822-H
$^{13}C_4{}^{15}N$-aspartate	Cambridge Isotope Laboratories	Cat# CNLM-544-H
3-isobutyl-1-methylxanthine (IBMX)	Sigma-Aldrich	Cat# CNLM-544-H
AKB	Sigma-Aldrich	Cat# K401
Antimycin A	Sigma-Aldrich	Cat# A8674
Aspartate	Sigma-Aldrich	Cat# A9256
Atpenin A5	Enzo	Cat# ALX-380-313
cOmplete protease inhibitor cocktail	Roche	Cat# 11873580001
Dexamethasone	Sigma-Aldrich	Cat# D4902
D-(+)-Glucose	Sigma-Aldrich	Cat# G7528
EmbryoMax Nucleoside mixture	Merck	Cat# ES-008-D

(*Continued on next page*)

Continued

REAGENT or RESOURCE	SOURCE	IDENTIFIER
FK866	Sigma-Aldrich	Cat# F8557
β-Glycerophosphate disodium salt hydrate	Sigma-Aldrich	Cat# G9422
Indomethacin	Sigma-Aldrich	Cat# I7378
Insulin solution from bovine pancreas	Sigma-Aldrich	Cat# I0516
L-Ascorbic Acid	Sigma-Aldrich	Cat# A4544
L-aspartic acid	Sigma-Aldrich	Cat# A9256
L-Glutamine	Gibco	Cat# 25030-024
PhenylmethanesulfonylFluoride (PMSF)	Sigma-Aldrich	Cat# P7626
Polybrene	Sigma-Aldrich	Cat# TR-1003
PhosSTOP phosphatase inhibitor cocktail	Roche	Cat# 04906837001
Puromycin	InvivoGen	Cat# ant-pr
Pyruvate	Gibco	Cat# 11360-039
Recombinant human transforming growth factor-β1	Peprotech	Cat# 100-21
Superscript II Reverse Transcriptase	Thermo Fisher Scientific	Cat# 18064022
SYBR GreenER qPCR SuperMix Universal	Thermo Fisher Scientific	Cat# 1178401K
Y-27632 (ROCK inhibitor)	Axon Medchem	Cat# 1683
Critical commercial assays		
Annexin V, APC conjugate (APC Annexin V)	Thermo Fisher Scientific	Cat# A35110
BCA Protein Assay Reagent	Thermo Fisher Scientific	Cat# 23225
CellTracker™ Green CMFDA Dye	Thermo Fisher Scientific	Cat# C7025
CM-H_2DCFDA	Thermo Fisher Scientific	Cat# C6827
DNeasy Blood & Tissue Kit	QIAGEN	Cat# 69504
FITC BrdU Flow Kit	BD Pharmingen	Cat# 559619
Global 5-hmC Quantification Kit	Active Motif	Cat# 55018
NucleoSpin RNA isolation kit	Machery Nagel	Cat# 740955
Deposited data		
Raw data	This manuscript; Mendeley	https://doi.org/10.17632/zc8f6f5s7n.1
DNA methylation/demethylation	This manuscript; GEO	GSE198222
Experimental models: Cell lines		
4T1	ATCC	CRL-2539 RRID:CVCL_0125
A549	ATCC	CRL-185 RRID:CVCL_0023
ROS 17/2.8	Dr. G. Rodan University of Connecticut US	RRID:CVCL_0508
NOMO-1	DSMZ	RRID:CVCL_1609
Experimental models: Organisms/strains		
Mouse: C57BL/6-ACTb-eGFP	Stiers et al., 2019	N/A
Mouse: *Tet2*$^{fl/fl}$	Moran-Crusio et al., 2011	N/A
Oligonucleotides		
Primer sequences for qRT-PCR - see Table S2	N/A	N/A
Puro cre empty vector	Addgene	Cat#17408, RRID:Addgene_17408
pLKO.1-puro Empty Vector Control Plasmid DNA	Sigma-Aldrich	Cat# SHC001
Mdh2 shRNA: CCGGCGGAATGCAC TTACTTCTCTACTCGAGTAGAGAAGT AAGTGCATTCCGTTTTTG	Sigma-Aldrich	Cat# SHCLNG-NM_008617
Software and algorithms		
Flowing Software	http://flowingsoftware.btk.fi/	RRID:SCR_015781
GraphPad Prism (version 8.3.0)	http://www.graphpad.com/	RRID:SCR_002798

(*Continued on next page*)

Continued

REAGENT or RESOURCE	SOURCE	IDENTIFIER
ImageJ software	https://imagej.nih.gov/ij/	RRID:SCR_003070
Xcalibur Software	Thermo Fisher Scientific	RRID:SCR_014593
Other		
Alcian Blue 8GX	Sigma-Aldrich	Cat# A5268
Alizarin Red S	Sigma-Aldrich	Cat# A5533
BIOTRANS(+) nylon membrane	MP Biomedicals	Cat# ICN810205
Collagenase type II	Gibco	Cat# 17101015
Dispase	Gibco	Cat# 17105041
Fetal bovine serum	Gibco	Cat# 10270106
Low melting point agarose	Lonza	Cat# 50115
New Methylene Blue N zinc chloride double salt	Sigma-Aldrich	Cat# 202096
Oil red O	Sigma-Aldrich	Cat# O0625
Penicillin/streptomycin	Gibco	Cat# 11548876
Trypsin-EDTA (0.05%)	Gibco	Cat# 25300054
Western Lightning Plus-ECL, Enhanced Chemiluminescence Substrate	PerkinElmer	Cat# NEL103E001EA

RESOURCE AVAILABILITY

Lead contact

Further information and requests for resources and reagents should be directed to and will be fulfilled by the lead contact, Geert Carmeliet (geert.carmeliet@kuleuven.be).

Materials availability

This study did not generate new unique reagents.

Data and code availability

- The raw data of DNA methylation/demethylation have been deposited on GEO and are publicly available as of the date of publication. Accession numbers are listed in the key resources table. Raw data of other experiments have been deposited on Mendeley and are publicly available as of the date of publication. DOI is listed in the key resources table. Microscopy data reported in this paper will be shared by the lead contact upon request.
- This paper does not report original code.
- Any additional information required to reanalyze the data reported in this work paper is available from the lead contact upon request.

EXPERIMENTAL MODEL AND SUBJECT DETAILS

Animals

C57BL/6, C57BL/6-ACTb-eGFP and *Tet2*$^{fl/fl}$ mice (Moran-Crusio et al., 2011) were bred in conventional conditions in our animal housing facility (Proefdierencentrum Leuven, Belgium) at 22°C under a 14-h light/10-h dark cycle, fed a normal chow diet (V1535; Ssniff GmbH, Soest, Germany). Rj:NMRI-Foxn1nu/nu mice were ordered from Janvier labs (Le Genest-Saint-Isle, France) and housed in the same conditions. Neonatal (5-day-old) C57BL/6 pups were used for the isolation of calvarial osteo-progenitors and growth plate chondrocytes. 8-week-old male and female C57BL/6, C57BL/6-ACTb-eGFP and *Tet2*$^{fl/fl}$ mice were used for the isolation of mPDCs and female Rj:NMRI-Foxn1nu/nu mice as host for the *in vivo* implantations. All animal experiments were conducted according to the regulations and with approval of the Animal Ethics Committee of the KU Leuven.

Cell lines

The four tumor cell lines (mouse female breast tumor cell line 4T1, human male lung carcinoma cell line A549, human female acute myeloid leukemia cell line NOMO-1 and rat osteosarcoma cell line ROS 17/2.8) were expanded in alpha-Minimum Essential Medium (αMEM) containing 5.5mM glucose, 1mM pyruvate and 0.22mM aspartate (Gibco, cat#32561) and supplemented with 2mM GlutaMAX, 10% FBS, 100U/ml penicillin and 100μg/ml streptomycin.

Primary cell culture

Cell isolation

To isolate murine periosteum-derived cells (mPDCs), tibiae and femora were dissected, surrounding muscles were removed and the epiphyses were embedded in 5% low melting point agarose (SeaPlaque; Lonza, Verviers, Belgium) (van Gastel et al., 2012). mPDCs were isolated from these bones, using a sequential digestion with a mixture of collagenase (3mg/ml) and dispase (4mg/ml; all from Gibco; Life Technologies, Ghent, Belgium) at 37°C in αMEM, containing 5.5mM glucose, 1mM pyruvate and 0.22 mM aspartate; supplemented with 2mM GlutaMAX, 100U/ml penicillin and 100μg/ml streptomycin (Gibco). Cells obtained after the first 10 min digest were discarded, whereas cells obtained after the second digest of 50 min were passed through a 70μm nylon mesh and plated in αMEM medium, supplemented with 2mM GlutaMAX, 10% FBS, 100U/ml penicillin and 100μg/ml streptomycin, referred as growth medium.

Primary growth plate chondrocytes were isolated as previously reported (Stegen et al., 2019). In brief, chondrocytes were isolated from growth plates of the proximal tibia and distal femur of 5-day-old mice. Isolated growth plates were pre-digested by constant agitation for 30 min at room temperature with collagenase type II (1mg/ml; Gibco) dissolved in growth medium. The remaining growth plate fragments were digested in collagenase type II (2mg/ml) for 3 h at 37°C. The primary chondrocytes obtained following the second digest were filtered through a 40μm nylon mesh and seeded at a density of 3×10^4 cells/cm^2.

Calvarial osteo-progenitors were isolated from 5-day-old mice as described previously (van Gastel et al., 2020). The cells were obtained by 6 sequential 15 min digestions of calvariae in PBS containing collagenase type II (1mg/ml) and dispase (2mg/ml). Cells isolated in fractions 2–6 were pooled and cultured in growth medium. To differentiate the obtained osteoprogenitors into more mature osteoblasts, cells were seeded at 3.5×10^3 cells/cm^2 and cultured for 3 days in osteogenic differentiation medium consisting of growth medium supplemented with 10mM β-glycerophosphate and 50μg/ml L-ascorbic acid (both from Sigma-Aldrich), whereafter they were trypsinized and seeded for experiment.

METHOD DETAILS

Cell culture

Treatment conditions

Primary skeletal cells or tumor cell lines were cultured in the presence of antimycin A (AMA) or vehicle as control. After one week, the cells were seeded at a density of 5.5×10^3 cells/cm^2 to investigate proliferation and survival in the presence or absence of AMA.

Concerning other mPDC treatments, pharmacological inhibitors were added either the day after mPDC isolation or the day after seeding mPDCs at 5.5×10^3 cells/cm^2. When performing nutrient deprivation, αMEM deprived of glucose, pyruvate or aspartate (custom-made media, Gibco) was added the day after seeding mPDCs at 5.5×10^3 cells/cm^2. The list and concentrations of chemicals used in this study are shown in Table S1.

Colony formation

For the *in vitro* fibroblastic colony-forming unit (CFU-F) assay, mPDCs were seeded at very low density (10 cells/cm^2) in Dulbecco's Modified Eagle Medium (DMEM; Gibco, cat#21969) containing high glucose (25mM) and supplemented with 15% FBS, 2mM glutamine, 100U/ml penicillin and 100μg/ml streptomycin (all from Gibco). After 10 days, the colonies were fixed with a solution of periodate-lysine-paraformaldehyde, stained with methylene blue (Sigma-Aldrich) and the number of colonies containing at least 20 cells was quantified (van Gastel et al., 2012).

Differentiation assays

For *in vitro* osteogenic differentiation, mPDCs were seeded at 25×10^3 cells/cm^2 in growth medium and cultured for 3 days to reach full confluence. Cells were then switched to osteogenic differentiation medium consisting of growth medium supplemented with 10mM β-glycerophosphate and 50μg/ml L-ascorbic acid (both from Sigma-Aldrich). After 10 days, cultures were stained for alkaline phosphatase (ALP) activity or mineral deposition (Alizarin Red) (Tournaire et al., 2020; van Gastel et al., 2012) or used for RNA isolation.

For chondrogenic differentiation, mPDCs were seeded at 25×10^3 cells/cm^2 in growth medium and switched after 3 days to chondrogenic differentiation medium consisting of growth medium supplemented with 10ng/ml recombinant human transforming growth factor-β 1 (Peprotech, Rocky Hill, CT, USA), 50μg/ml L-ascorbic acid and 20μM Y-27632 (ROCK inhibitor, Axon Medchem, Groningen, The Netherlands). After 10 days, cultures were stained for glycosaminoglycans (Alcian Blue 8GX; Sigma-Aldrich) (Tournaire et al., 2020; van Gastel et al., 2012) or used for RNA isolation.

For adipogenic differentiation, mPDCs were seeded 10×10^3 cells/cm^2 in growth medium for 3 days and then switched to adipogenic differentiation medium consisting of growth medium supplemented with 10nM dexamethasone, 50μM indomethacin, 10μg/ml insulin and 500nM IBMX (all from Sigma-Aldrich). After 10 days cells were stained for presence of lipid droplets (Oil Red O; Sigma-Aldrich) (Tournaire et al., 2020; van Gastel et al., 2012) or used for RNA isolation.

Genetic targeting

To silence *Mdh2*, mPDCs were transduced, in the presence of 8μg/ml polybrene (Sigma-Aldrich, Diegem, Belgium) with a lentivirus carrying the gene-targeting shRNA (Sigma-Aldrich) the day after isolation. A lentivirus containing an empty vector (Sigma-Aldrich) was used as negative control. To silence *Tet2*, cells isolated from *Tet2*$^{fl/fl}$ mice and wild-type (*Tet2*$^{wt/wt}$) littermates were transduced

with a lentivirus carrying a Puro.Cre empty vector (Addgene, Watertown, MA, USA). After 72h, puromycin (2μg/ml; InvivoGen, San Diego, CA, USA) was added to the culture medium for 48h. Sequences of the shRNAs are listed in Table S2.

Flow cytometry analysis and cell sorting

Stem cell and progenitor markers

Freshly isolated or expanded mPDCs were suspended in Hank's Balanced Salt Solution (HBSS from Gibco) supplemented with 2% FBS and 2mM EDTA. The cells were incubated for 15 min at 4°C with specific antibodies at the indicated concentration (Table S3). The stromal fraction of freshly isolated mPDCs was defined as $CD31^-/CD45^-/Ter119^-/CD51^+$, the skeletal stem cells (SSCs) as $CD31^-/CD45^-/Ter119^-/CD51^+/CD90^-/CD105^-/BP1^-/CD200^+$ and the pre-bone/cartilage/stromal progenitors (pre-BCSPs) as $CD31^-/CD45^-/Ter119^-/CD51^+/CD90^-/CD105^-/BP1^-/CD200^-$ (Chan et al., 2015).

Cell viability

In vitro and *ex vivo* cell viability was evaluated by Annexin V allophycocyanin (1/20; APC) conjugate and 1μg/ml Propidium Iodide (AnxV-PI, both from Invitrogen, Thermo Fisher Scientific). The $AnxV^-PI^-$ cell population was considered as viable.

Cell proliferation

To investigate proliferation, 10μM BrdU was added to the mPDCs for 12h and to the tumor cell lines for 4h and its incorporation was measured by using the FITC BrdU Flow Kit (BD Pharmingen, Erembodegem, Belgium) according to the manufacturer's instructions.

All flow cytometry analyses were performed on a Gallios Flow Cytometer (Beckman Coulter, Brea, USA) and analyzed by Flowing Software (University of Turku, Turku, Finland).

RNA extraction and quantitative real-time (qRT)-PCR

Total RNA was extracted using the Nucleospin RNA isolation Kit (Macherey-Nagel GmbH, Duren, Germany) according to the manufacturer's instructions. Reverse transcription was performed using Superscript II Reverse Transcriptase (Invitrogen, Thermo Fisher Scientific) and the analysis of quantitative reverse transcriptase polymerase chain reaction (qRT-PCR) was performed on the StepOnePlus Real-Time PCR System (Applied Biosystems, Thermo Fisher Scientific) using specific forward and reverse oligonucleotide primers with SYBR Green or with fluorescent dye (FAM) and quencher (TAMRA) when a probe was used (Table S2). Expression levels were normalized for the expression of the murine housekeeping gene hypoxanthine-guanine phosphoribosyl transferase (*mHprt*) and analyzed using the $2^{-\Delta\Delta CT}$ method.

Western blot

Total cell lysates were obtained by lysing the cells in 62.5mM Tris buffer (pH 6.8) containing 10% glycerol, 2% SDS, 1x cOmplete proteinase inhibitor cocktail (Roche, Basel, Switzerland) and 1x PhosSTOP phosphatase inhibitor cocktail (Roche). To obtain the nuclear protein fraction, cells were lysed in a hypotonic buffer (20mM Hepes pH 7.9, 10mM KCl, 1.5mM $MgCl_2$, 1mM EDTA, 0.5% NP40, 1mM DTT, supplemented with 1mM Na_3VO_4, 20mM NaF, 1mM PMSF, 5μg/ml aprotinin, 5μg/ml leupeptin and 0.33μg/ml antipain) for 15 min at 4°C, followed by mechanical disruption of the cell membranes. Nuclei were pelleted from the lysates by centrifugation and the pellet was resuspended in a nuclear extraction buffer (50mM Hepes pH 7.9, 500mM NaCl, 1% NP40, supplemented with 1mM PMSF, 5μg/ml aprotinin, 5μg/ml leupeptin and 0.33μg/ml antipain), sonicated and incubated for 15 min at 4°C. Protein concentrations were determined with the Pierce™ BCA Protein Assay Kit (Thermo Fisher Scientific).

Proteins were separated by SDS–PAGE under reducing conditions and transferred to a nitrocellulose membrane (GE Healthcare). Membranes were blocked with 5% dry milk or bovine serum albumin (Sigma-Aldrich) in Tris-buffered saline with 0.1% Tween-20 for 60 min at room temperature and incubated overnight at 4°C with primary antibodies (Table S3). Signals were detected by enhanced chemiluminescence (Western Lightning Plus ECL; PerkinElmer, Waltham, MA, USA) after incubation with appropriate HRP-conjugated secondary antibodies (Table S3). Protein levels were quantified relative to loading control.

DNA methylation/hydroxymethylation analysis

5-hydroxymethylcytosine (5hmC) dot blot

Genomic DNA was isolated using DNeasy Blood & Tissue Kit (Qiagen, Hilden, Germany). Isolated DNA (2μg) was denatured in 0.4M NaOH and 10mM EDTA for 10 min at 100°C. The samples were loaded on Biotrans(+) Transfer Membrane (MP Biomedical, Irvine, CA, USA) by using a Minifold vacuum-assisted dot blot apparatus (Whatman, GE Healthcare, Chicago, IL, USA). The membrane was rinsed with 2x saline sodium citrate buffer and DNA was immobilized by UV crosslinking using the Stratalinker 1800 (Stratagene, San Diego, CA, USA). The membrane was then blocked with 5% dry milk in Tris-buffered saline with 0.1% Tween 20 for 60 min at room temperature and incubated overnight at 4°C with primary anti-5hmC antibody (Table S3). Signals were detected by enhanced chemiluminescence (Western Lightning Plus ECL; PerkinElmer) after incubation with HRP-conjugated Goat Anti-Rabbit antibodies (Dako, Agilent Technologies, Santa Clara, CA, USA). Loading of spotted DNA was analyzed by staining the membrane with 0.02% methylene blue.

5hmC ELISA

To quantify 5hmC levels in genomic DNA, a Global 5hmC quantification kit (Active Motif, La Hulpe, Belgium) was used according to manufacturer's instructions.

DNA methylation/demethylation analysis

To analyze DNA methylation/demethylation in 3 pools of mPDCs treated with vehicle or AMA for 10 days, DNA was extracted from cell lysates using silica columns following manufacturer's instructions (DNeasy Blood and Tissue kit, Qiagen), followed by RNASE H and Proteinase K treatment and an additional purification using solid phase reversible immobilisation (AMPure XP, Beckman Coulter). DNA was next converted using the oxidative bisulfite or normal bisulfite method as described previously (De Borre and Branco, 2021), and hybridized to Illumina mouse EPIC Beadchip arrays (Life & Brain, Bonn, Germany). The resultant.idat files were analyzed using the minfi package. Methylation state distributions were analyzed as an initial quality control. Next, low-quality CpGs were excluded, before background correction. Raw data from bisulfite-chip and oxidative bisulfite-chip were each batch-normalized using inter-array quantile normalization, and converted to beta values using the ENmix R package. The Infinium Mouse Methylation v1.0 A1 manifest file was used for CpG annotation. CpGs showing significant levels of cytosine hydroxymethylation were identified using limma as those containing significantly more (1% false-discovery rate) signal following bisulfite-chip versus oxidative bisulfite-chip across all 6 samples. Differential DNA methylation between AMA- and veh-treated cells at probes showing significant 5hmC levels was determined by fitting multiple linear models by weighted or generalized least squares, using limma.

Metabolic analyses

Oxygen consumption rate (OCR)

OCR was quantified by an XF24 analyzer (Seahorse Bioscience, North Billerica, MA, USA) on cells seeded on Seahorse XF24 tissue culture plates (50×10^3 cells per well) in unbuffered DMEM medium (D5030) supplemented with 5mM glucose and 2mM glutamine, pH7.4 (all from Gibco). OCR was measured every 6 min during 96 min. At 24 min Oligomycin A (1.24μM) was added to inhibit ATP synthase reducing OCR linked to cellular ATP production. The uncoupler 2,4-dinitrophenol (DNP) (100μM) was added at 48 min to evaluate the maximum respiration of the cells. 1μM AMA was finally added to the cells at 72 min (all from Sigma-Aldrich). Values were normalized to DNA content.

Lactate and glucose

Lactate and glucose concentrations in culture medium were measured using a Beckman Coulter analyzer AU640 (Beckman Coulter) and normalized to DNA content.

Glycolytic flux

To measure glycolytic flux, cells were incubated in growth medium containing 0.4μCi/ml [5-^{3}H]-D-glucose (PerkinElmer). After 2h, the culture medium was transferred into glass vials sealed with rubber caps and ^3H_2O was captured in hanging wells containing a Whatman paper soaked with H_2O over a period of 48h at 37°C. Radioactivity was determined in the paper by liquid scintillation counting and normalized to protein content.

Mass spectrometry

To measure metabolites and coenzymes, cells were rinsed with ice-cold 0.9% NaCl solution and scraped in ice-cold extraction buffer (80% methanol in AD, supplemented with 2μM d27 myristic acid). The metabolites were collected in the supernatant fraction and measured using liquid chromatography-mass spectrometry (LC-MS). For medium analysis, 10μL medium was added to 990μL extraction buffer. After an overnight storage at −80°C, the solution was centrifuged and the supernatant was analyzed by LC-MS. To trace the contribution of glucose, glutamine, pyruvate or aspartate to other metabolites, cells were cultured for 72h in glucose-free, glutamine-free, pyruvate-free or aspartate-free αMEM (custom media, Gibco) supplemented with dialyzed FBS and $^{13}C_6$-glucose, [3,4]-$^{13}C_2$-glucose, $^{13}C_5$-glutamine, $^{13}C_3$-pyruvate or $^{13}C_4$-^{15}N-aspartate (all from Cambridge Isotope Laboratories, Tewksbury, MA, USA). The incorporation of carbons derived from glucose, glutamine, pyruvate or aspartate was analyzed using LC-MS. LC-MS runs were performed by the VIB Metabolomics Core (Leuven, Belgium), analyzed using Xcalibur Software (ThermoFisher) and normalized to protein content. When referring to metabolite contribution in figures, we show either (i) the fractional contribution, calculated based on the following equation (Buescher et al., 2015):

$$\text{total contribution of carbon} = \frac{\sum_{i=0}^{n} i * m_i}{n * \sum_{i=0}^{n} m_i}$$

where n is the number of C atoms in the metabolite, i represents the different mass isotopomers and m refers to the abundance of a certain mass or (ii) relevant mass distribution vectors, specified in the figure legends.

Mouse model of bone regeneration

In order to investigate the *in vivo* osteogenic potential of mPDCs, an ectopic bone formation model was used (Stegen et al., 2016). Briefly, 1×10^6 mPDCs were seeded on a $3 \times 3 \times 3$ mm^3 calcium phosphate-collagen scaffold (NuOss™ collagen, ACE Surgical Supply, Brockton, MA, USA). After overnight incubation, scaffolds were implanted subcutaneously on the back of 8-week old Rj:NMRI-Foxn1nu/nu mice, near blood vessels. Mice were anesthetized by peritoneal injection of a mixture of 100mg/kg ketamine and 15mg/kg xylazine in saline. After 8 weeks, scaffolds were isolated and bone formation was assessed by (immuno)histochemical stainings on paraffin- or cryo-sections.

To study cell survival and colony formation of the donor cells after *in vivo* implantation, the cells were labeled with CellTracker™ Green CMFDA (Invitrogen, Thermo Fisher Scientific) prior to seeding them on the scaffold. Three days after implantation, the

scaffolds were isolated and the cells released using a mixture of 3mg/ml collagenase type II and 4mg/ml dispase in αMEM for 20 min. $CD31^-/CD45^-/Ter119^-/CMFDA^+$ cells were sorted by flow cytometry (BD FACSAria III, BD Biosciences, Erembodegem Belgium). Cell survival was investigated on sorted cells using AnxV-PI flow-cytometry analysis. Colony formation was analyzed by seeding isolated donor cells at 500 cells/cm^2 in growth medium without addition of AMA and culturing them for one week.

(Immuno)histochemistry

Isolated scaffolds were fixed overnight in 2% paraformaldehyde at 4°C and decalcified in EDTA (0.5M; pH 7,4) for 14 days at 4°C. Scaffolds implanted with mPDCs derived from C57BL/6 mice were dehydrated, embedded in paraffin and sectioned at 4 μm. Scaffolds implanted with mPDCs derived from C57BL/6-ACTb-eGFP mice were embedded in NEG-50 frozen section medium (Richard-Allen Scientific, Thermo Fisher Scientific), and sectioned with a cryostat at 7μm. Hematoxylin and eosin (H&E) staining as well as immunohistochemical stainings were performed as described previously (Stegen et al., 2016; Stiers et al., 2019; Tournaire et al., 2020). Antibodies used are listed in Table S3. Images were taken on a Zeiss Axioplan 2 light microscope (Carl Zeiss Microscopy GmbH, Jena, Germany). Quantification of the newly formed bone in the implanted scaffolds was performed by manual outlining areas of bone and total tissue. The quantification of the area and number of blood vessels relative to the scaffold area was performed by counting or outlining CD31-positive vessels with a clear lumen. These histomorphometric analyses were performed using Axiovision software (v6.1.0). The quantification of cells that were double-positive for β-actin-GFP and Osterix was performed manually by using the ImageJ software (NIH, Bethesda, MD, USA; https://imagej.nih.gov/ij/).

QUANTIFICATION AND STATISTICAL ANALYSIS

Data are presented as mean ± SD and analyzed by two-tailed Student's t-test or one-way, two-way, three-way ANOVA with Tukey-Kramer post-hoc test using the GraphPad Prism software (GraphPad Software, San Diego, CA, USA). The results of two-way and three-way ANOVA are shown in Table S4. The analysis of DNA methylation/demethylation was performed using Fisher's exact test and Wilcoxon signed rank test with continuity correction. The number of biological replicates are represented by n values. For immunoblots, representative images are shown of at least three independent experiments. Differences were considered statistically significant at $p < 0.05$.

Cell Reports, Volume *40*

Supplemental information

Skeletal progenitors preserve proliferation and self-renewal upon inhibition of mitochondrial respiration by rerouting the TCA cycle

Guillaume Tournaire, Shauni Loopmans, Steve Stegen, Gianmarco Rinaldi, Guy Eelen, Sophie Torrekens, Karen Moermans, Peter Carmeliet, Bart Ghesquière, Bernard Thienpont, Sarah-Maria Fendt, Nick van Gastel, and Geert Carmeliet

Figure S1

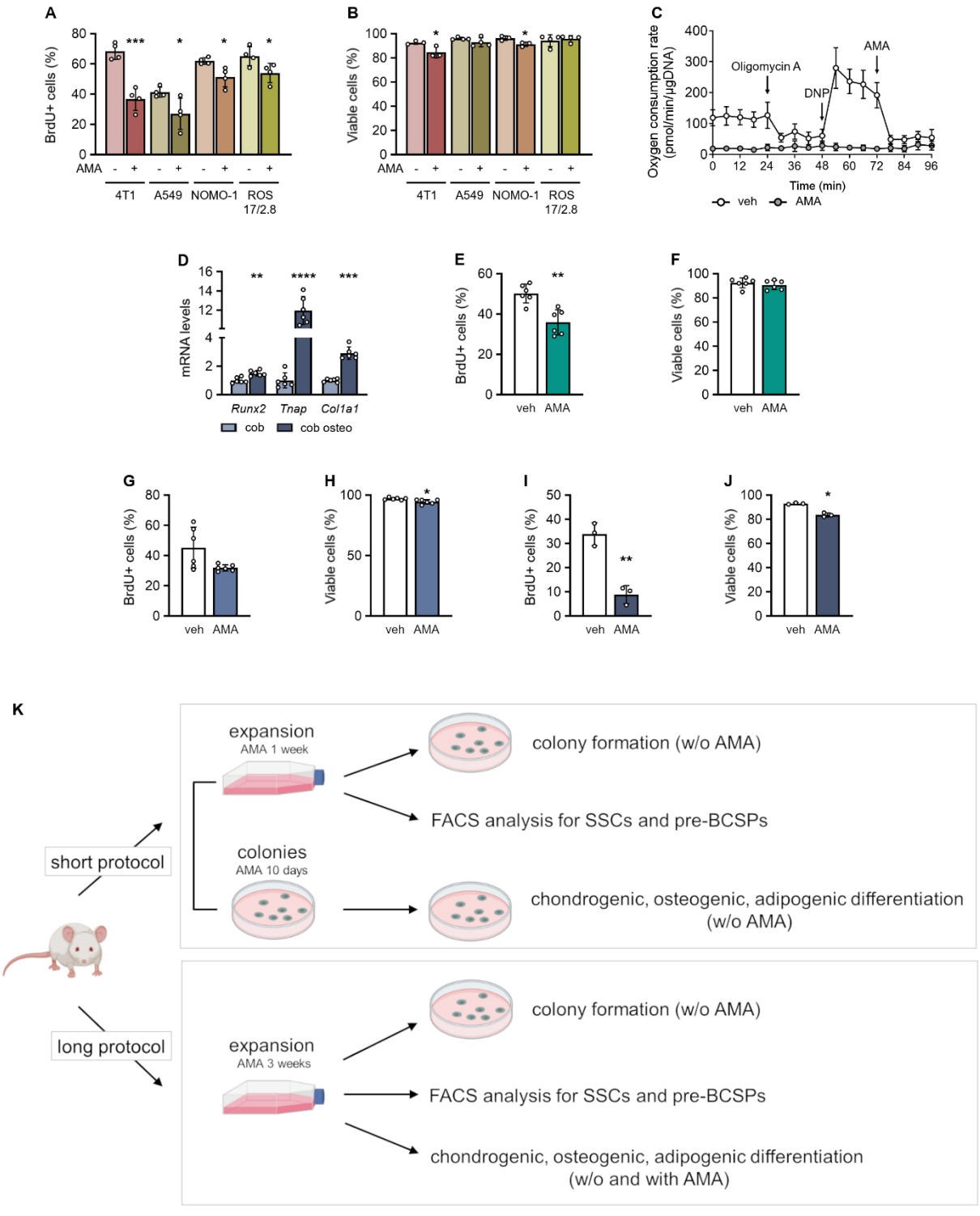
A
BrdU+ cells (%)
AMA
4T1
A549
NOMO-1
ROS 17/2.8
B
Viable cells (%)
C
Oxygen consumption rate (pmol/min/µgDNA)
Oligomycin A
DNP
AMA
Time (min)
veh
AMA
D
mRNA levels
Runx2
Tnap
Col1a1
cob
cob osteo
E
F
G
H
I
J
K
expansion
AMA 1 week
colony formation (w/o AMA)
FACS analysis for SSCs and pre-BCSPs
colonies
AMA 10 days
chondrogenic, osteogenic, adipogenic differentiation (w/o AMA)
short protocol
long protocol
expansion
AMA 3 weeks
colony formation (w/o AMA)
FACS analysis for SSCs and pre-BCSPs
chondrogenic, osteogenic, adipogenic differentiation (w/o and with AMA)

Figure S1. Effect of AMA on tumor cell lines and periosteal cells and strategy to investigate the effect of AMA on SSPC properties, related to Figure 1.

(A) Flow cytometry analysis of BrdU positive ($BrdU^+$) 4T1, A549, NOMO-1and ROS 17/2.8 cancer cells treated with vehicle (veh) or 10µM Antimycin A (AMA) for 7 days (n=4).

(B) Cell viability, using Annexin V-Propidium Iodide flow cytometry, of 4T1, A549, NOMO-1and ROS 17/2.8 cancer cells treated with veh or AMA for 7 days (n=3-4).

(C) Oxygen consumption rate in veh- and AMA-treated mouse periosteal cells (2,4-dinitrophenol, DNP; n=3).

(D) Culturing calvarial osteoblasts (cob) for 3 days in osteogenic differentiation medium (cob osteo) results in mature osteoblasts, assessed by quantification of *Runx2*, *Tnap* and *Col1a1* mRNA levels (n=6).

(E) Flow cytometry analysis of $BrdU^+$ growth plate chondrocytes treated with veh or 10µM AMA for 24h (n=6).

(F) Cell viability, using Annexin 0V-Propidium Iodide flow cytometry, of growth plate chondrocytes treated with veh or AMA for 24h (n=6).

(G) Flow cytometry analysis of $BrdU^+$ calvarial cells treated with veh or AMA for 24h (n=6).

(H) Cell viability, using Annexin V-Propidium Iodide flow cytometry, of calvarial cells treated with veh or AMA for 24h (n=6).

(I) Flow cytometry analysis of $BrdU^+$ mature osteoblasts (cob osteo) treated with veh or 10µM AMA for 24h (n=3).

(J) Cell viability, using Annexin V-Propidium Iodide flow cytometry, of mature osteoblasts (cob osteo) treated with veh or AMA for 24h (n=3).

(K) Schematic representation of experimental design to investigate SSPC properties. The effect of AMA treatment on SSPC properties was determined using a short or long protocol. In the short protocol, periosteal cells were expanded for 1 week with vehicle or AMA and their capacity to form colonies, in the absence of AMA, as well as the percentage of skeletal stem cells (SSCs) and pre-bone, cartilage and stromal progenitors (pre-BCSPs) was investigated. In parallel, freshly isolated cells were seeded at clonal density and treated with AMA for 10 days. AMA treatment was stopped and colonies were further cultured in medium inducing chondrogenic, osteogenic or adipogenic differentiation to investigate their tri-lineage potential.
In the long protocol, we expanded cells for 3 weeks, corresponding to 3 passages, with vehicle or AMA and analyzed their capacity to form colonies, the percentage of SSCs and pre-BCSPs and their tri-lineage differentiation potency in the presence or absence of AMA.

Data are means ± SD. *$p<0.05$, **$p<0.01$, ***$p<0.001$, ****$p<0.0001$ vs veh (two-tailed Student's *t*-test).

Figure S2

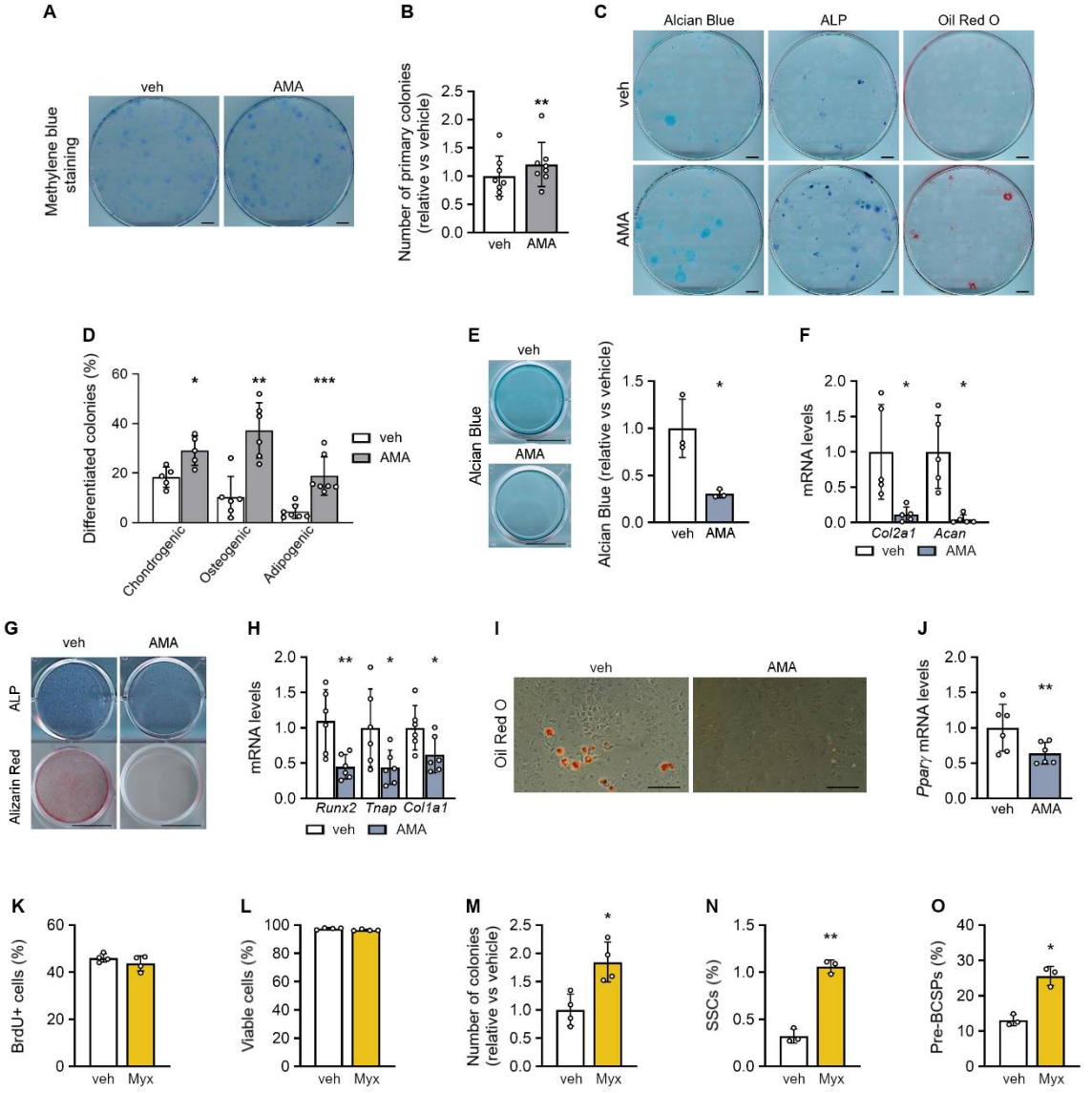

Figure S2. AMA treatment during expansion of SSPCs preserves their multilineage potential, but has negative effects when used during differentiation, related to Figure 1.
(A and B) Visualization (A, Methylene blue staining) and quantification of the number of colonies formed after culture of SSPCs with vehicle (veh; control) or 10µM Antimycin A (AMA) for 10 days (B, n=8).
(C and D) Visualization of chondrogenic, osteogenic and adipogenic differentiation of colonies (C) and quantification of the number of colonies (D) staining positive respectively for the presence of chondrogenic matrix (Alcian blue; n=5), alkaline phosphatase activity (ALP; n=6) or lipid deposits (Oil Red O; n=7). Colonies were formed in the presence of veh or AMA, but differentiated in the absence of AMA.
(E and F) Chondrogenic differentiation in the presence of veh (control) or AMA, assessed by visualization and quantification of chondrogenic matrix deposition (Alcian blue staining) (E; n=3) and quantification of *Col2a1* and *Acan* mRNA levels (F; n=5).
(G and H) Osteogenic differentiation in the presence of veh or AMA, assessed by visualization of alkaline phosphatase activity (ALP) and mineralized matrix deposition (Alizarin red staining) (G; n=3) and quantification of *Runx2*, *Tnap*, *Col1a1* mRNA levels (H; n=6).
(I and J) Adipogenic differentiation in the presence of veh or AMA, assessed by visualization of lipid deposits (Oil Red O staining) (I; n=4) and quantification of *Pparγ* mRNA levels (J; n=6).
(K) Flow cytometry analysis of $BrdU^+$ SSPCs treated with veh or 10µM Myxothiazol (Myx) for 7 days (n=4).
(L) Cell viability, using Annexin V-Propidium Iodide flow cytometry, of SSPCs treated with veh or Myx (n=4).

(M) Number of colonies formed after culture of SSPCs with veh (control) or Myx (n=4).
(N and O) Flow cytometry analysis of the percentage of skeletal stem cells (SSCs, N) and pre-bone, cartilage and stromal progenitors (pre-BCSPs, O) in veh- or Myx-treated cells (n=3).
Data are means ± SD. *p<0.05, **p<0.01, ***p<0.001 vs veh (paired two-tailed Student's *t*-test). Scale bar in A, C, E, G: 1 cm; in I: 200 μm.

Figure S3

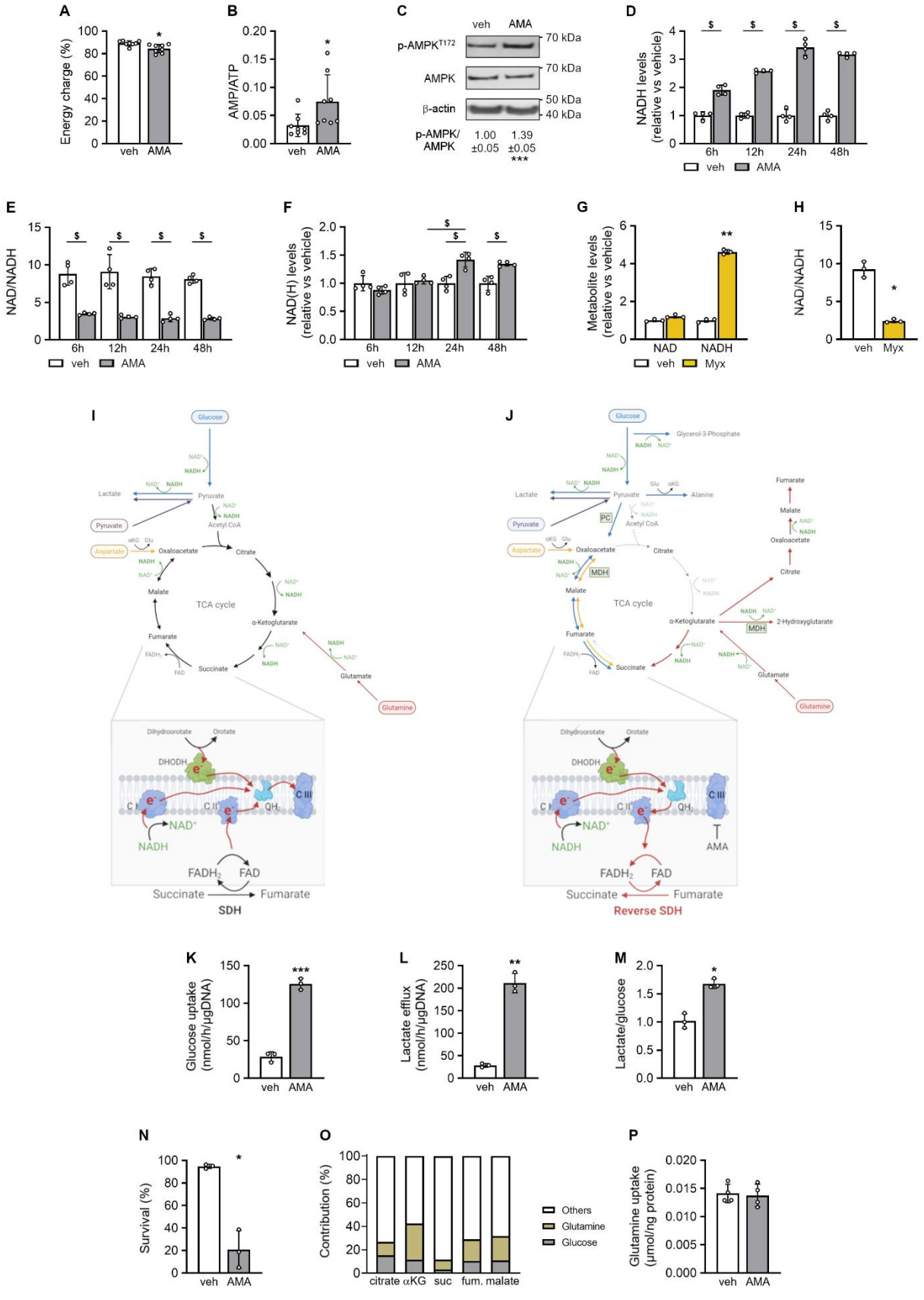
A
Energy charge (%)
veh AMA
B
AMP/ATP
veh AMA
C
veh AMA
p-AMPK^{T172}
AMPK
β-actin
70 kDa
70 kDa
50 kDa
40 kDa
p-AMPK/ AMPK
1.00 ±0.05
1.39 ±0.05
***
D
NADH levels (relative vs vehicle)
6h 12h 24h 48h
veh AMA
E
NAD/NADH
6h 12h 24h 48h
veh AMA
F
NAD(H) levels (relative vs vehicle)
6h 12h 24h 48h
veh AMA
G
Metabolite levels (relative vs vehicle)
NAD NADH
veh Myx
H
NAD/NADH
veh Myx
I
Glucose
Lactate
Pyruvate
Acetyl CoA
Aspartate
Oxaloacetate
Citrate
Malate
TCA cycle
α-Ketoglutarate
Fumarate
Succinate
Glutamate
Glutamine
Dihydroorotate
Orotate
DHODH
C I
C II
C III
QH$_2$
NAD$^+$
NADH
FADH$_2$
FAD
Succinate
Fumarate
SDH
J
Glucose
Glycerol-3-Phosphate
Lactate
Pyruvate
Glu
αKG
Alanine
PC
Acetyl CoA
Aspartate
Oxaloacetate
MDH
Citrate
Malate
Fumarate
TCA cycle
α-Ketoglutarate
2-Hydroxyglutarate
Succinate
Glutamate
Glutamine
Dihydroorotate
Orotate
DHODH
C I
C II
C III
QH$_2$
NAD$^+$
NADH
AMA
FADH$_2$
FAD
Succinate
Fumarate
Reverse SDH
K
Glucose uptake (nmol/h/μgDNA)
veh AMA
L
Lactate efflux (nmol/h/μgDNA)
veh AMA
M
Lactate/glucose
veh AMA
N
Survival (%)
veh AMA
O
Contribution (%)
citrate αKG suc fum. malate
Others
Glutamine
Glucose
P
Glutamine uptake (μmol/ng protein)
veh AMA

Figure S3. SSPCs are in energy stress despite increased glycolysis and they increase the NAD(H) pool to preserve proliferation upon ETC inhibition, related to Figure 2.

(A and B) Energy charge calculated as ([ATP] + ½ [ADP])/([ATP]+ [ADP]+ [AMP]) (A; n=8) and AMP to ATP ratio (B; n=8) in cells treated with vehicle (veh) or 10μM Antimycin A (AMA).

(C) Immunoblot of p-AMPK^{T172}, AMPK, and β-actin with quantification of p-AMPK^{T172} to AMPK ratio in veh- and AMA-treated cells. Representative images of 3 experiments are shown.

(D-F) NADH levels (D; n=4), NAD/NADH ratio (E; n=4) and NAD + NADH (NAD(H)) levels (F; n=4) in cells treated with veh (control) or AMA for indicated time points.

(G and H) NAD and NADH levels (G; n=3) and NAD/NADH ratio (H; n=3) in cells treated with veh (control) or 10μM Myxothiazol (Myx) for 3 days.

(I) Schematic representation showing pathways that produce NADH in veh-treated cells or that regenerate NAD^+ by converting pyruvate to lactate and by transferring electrons (e^-) to the electron transfer chain (ETC). (DHODH: dihydroorotate dehydrogenase; C I: complex I of ETC; C II: complex II; C III: complex III; QH_2: ubiquinol; SDH: succinate dehydrogenase)

(J) Schematic representation showing metabolic adaptations in AMA-treated cells: pathways producing NADH are downregulated, including pyruvate dehydrogenase (PDH) and the conversion of citrate to □-ketoglutarate in the TCA cycle, while pathways that can regenerate NAD^+ are stimulated, including the conversion of glucose to glycerol-3-phosphate, of α-Ketoglutarate to 2-Hydroxyglutarate and of Oxaloacetate to Malate. In addition, reverse SDH activity allows that electrons are still transferred from C I and DHODH to QH2. Thin dashed arrows indicate downregulation (Glu: Glutamate; αKG, α-Ketoglutarate; MDH: malate dehydrogenase).

(K-M) Glucose uptake (K; n=3), lactate efflux (L; n=3) and ratio of lactate efflux to glucose uptake (M; n=3) in veh- and AMA-treated cells.

(N) Cell viability of veh- and AMA-treated cells cultured for 24h in glucose-deprived medium (0,5mM) and analyzed by Annexin V-Propidium Iodide flow cytometry (n=3).

(O) Fractional contribution of $^{13}C_5$-glutamine and $^{13}C_6$-glucose to citrate, αKG, succinate (suc), fumarate (fum) and malate in periosteal cells (n=8).

(P) Consumption of glutamine during 24h by veh- and AMA-treated cells (n=4).

Data are means ± SD. *p<0.05, **p<0.01, ***p<0.001 vs veh (paired two-tailed Student's *t*-test), $^{\$}$p<0.05 (two-way ANOVA).

Figure S4

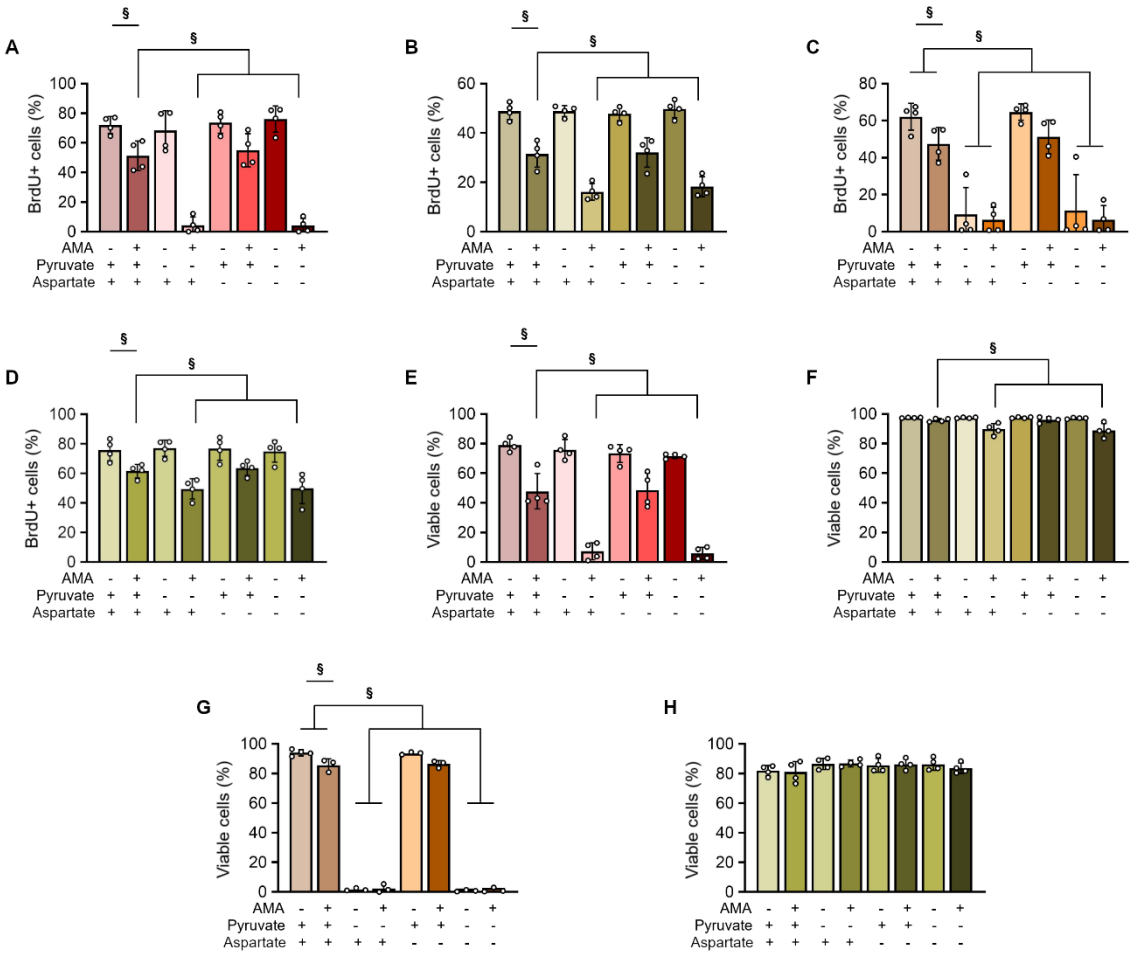

Figure S4. Tumor cells rely on pyruvate upon AMA-treatment, related to Figure 3.
(A-D) Flow cytometry analysis of BrdU positive ($BrdU^+$) 4T1 (A; n=4), A549 (B; n=4), NOMO-1 (C; n=4) and ROS 17/2.8 (D; n=4) cancer cells treated with vehicle (veh) or 10µM Antimycin A (AMA) for 7 days and then for 24h in medium with 1mM pyruvate and 0.22mM aspartate or without pyruvate and/or aspartate.
(E-H) Cell viability, using Annexin V-Propidium Iodide flow cytometry, of 4T1 (E; n=4), A549 (F; n=4), NOMO-1 (G; n=3) and ROS 17/2.8 (H; n=4) cancer cells treated with veh or 10µM AMA for 7 days and then for 24h in medium with 1mM pyruvate and 0.22mM aspartate or without pyruvate and/or aspartate.
Data are means ± SD. $^{\S}p<0.05$ (three-way ANOVA).

Figure S5

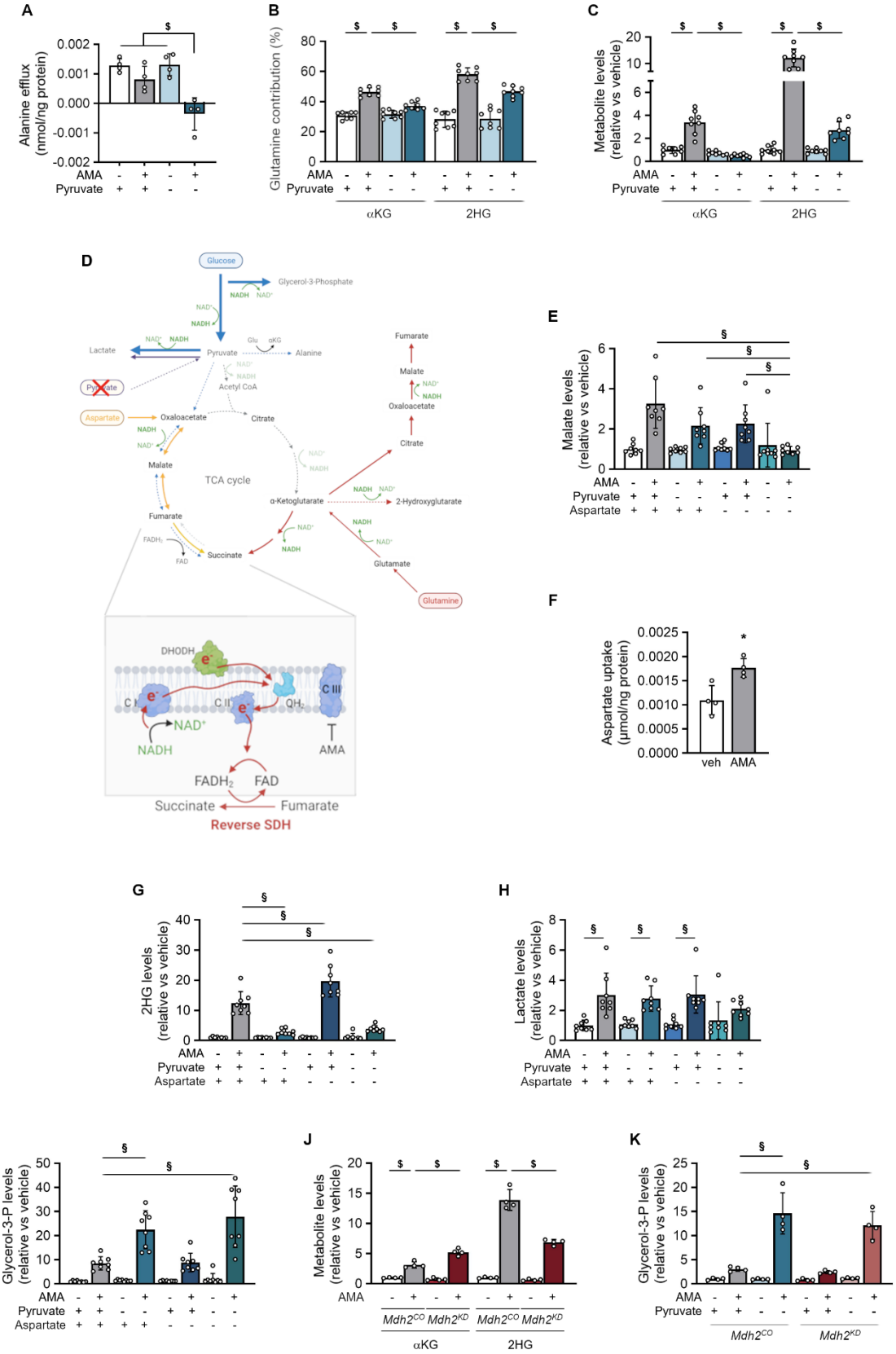
A
Alanine efflux (nmol/ng protein)
AMA
Pyruvate
B
Glutamine contribution (%)
αKG
2HG
C
Metabolite levels (relative vs vehicle)
D
Glucose
Glycerol-3-Phosphate
Lactate
Pyruvate
Alanine
Acetyl CoA
Aspartate
Oxaloacetate
Citrate
Malate
TCA cycle
Fumarate
α-Ketoglutarate
2-Hydroxyglutarate
Succinate
Glutamate
Glutamine
DHODH
C I
C II
C III
QH2
NAD+
NADH
FADH2
FAD
AMA
Succinate
Fumarate
Reverse SDH
E
Malate levels (relative vs vehicle)
Aspartate
F
Aspartate uptake (µmol/ng protein)
veh
AMA
G
2HG levels (relative vs vehicle)
H
Lactate levels (relative vs vehicle)
I
Glycerol-3-P levels (relative vs vehicle)
J
Metabolite levels (relative vs vehicle)
Mdh2CO
Mdh2KD
K
Glycerol-3-P levels (relative vs vehicle)

Figure S5: Extracellular pyruvate and aspartate promote NAD^+ regeneration, related to Figure 3.
(A) Alanine efflux during 24h by cells treated with vehicle (veh) or 10μM Antimycin A (AMA) (n=4)
(B) Fractional contribution of $^{13}C_5$-glutamine to α-ketoglutarate (αKG) and 2-hydroxyglutarate (2HG) in veh- and AMA-treated cells cultured with or without 1mM pyruvate (n=8)
(C) αKG and 2HG levels in veh (control)- and AMA-treated cells cultured with or without pyruvate (n=8).
(D) Schematic representation of metabolic adaptations in AMA-treated cells cultured in pyruvate-deprived condition. Pyruvate deprivation decreases the contribution of glucose to malate and the conversion of glucose to alanine, thereby reducing the production of αKG and indirectly of 2HG, which could affect NAD^+ regeneration. NAD^+ levels are nevertheless maintained by increased glucose contribution to glycerol-3-phosphate (glycerol-3-P). Thick arrows indicate upregulation, thin dashed arrows downregulation.
(E) Malate levels in veh (control)- and AMA-treated cells cultured in medium with 1mM pyruvate and 0.22mM aspartate or without pyruvate and/or aspartate (n=8).
(F) Aspartate consumption during 24h by veh- and AMA-treated cells (n=4).
(G-I) 2HG (G), Lactate (H) and glycerol-3-P(I) levels in veh (control)- and AMA-treated cells cultured in medium with 1mM pyruvate and 0.22mM aspartate or without pyruvate and/or aspartate (n=8).
(J) αKG and 2HG levels in veh (control)- and AMA-treated cells transduced with control ($Mdh2^{CO}$) or MDH2-specific shRNA ($Mdh2^{KD}$) (n=4).
(K) Glycerol-3-P levels in veh (control)- and AMA-treated $Mdh2^{CO}$ and $Mdh2^{KD}$ cells cultured with or without pyruvate (n=4).
Data are means ± SD. *p<0.05 (paired two-tailed Student's *t*-test), $^{\$}$p<0.05 (two-way ANOVA), §p<0.05 (three-way ANOVA).

Figure S6

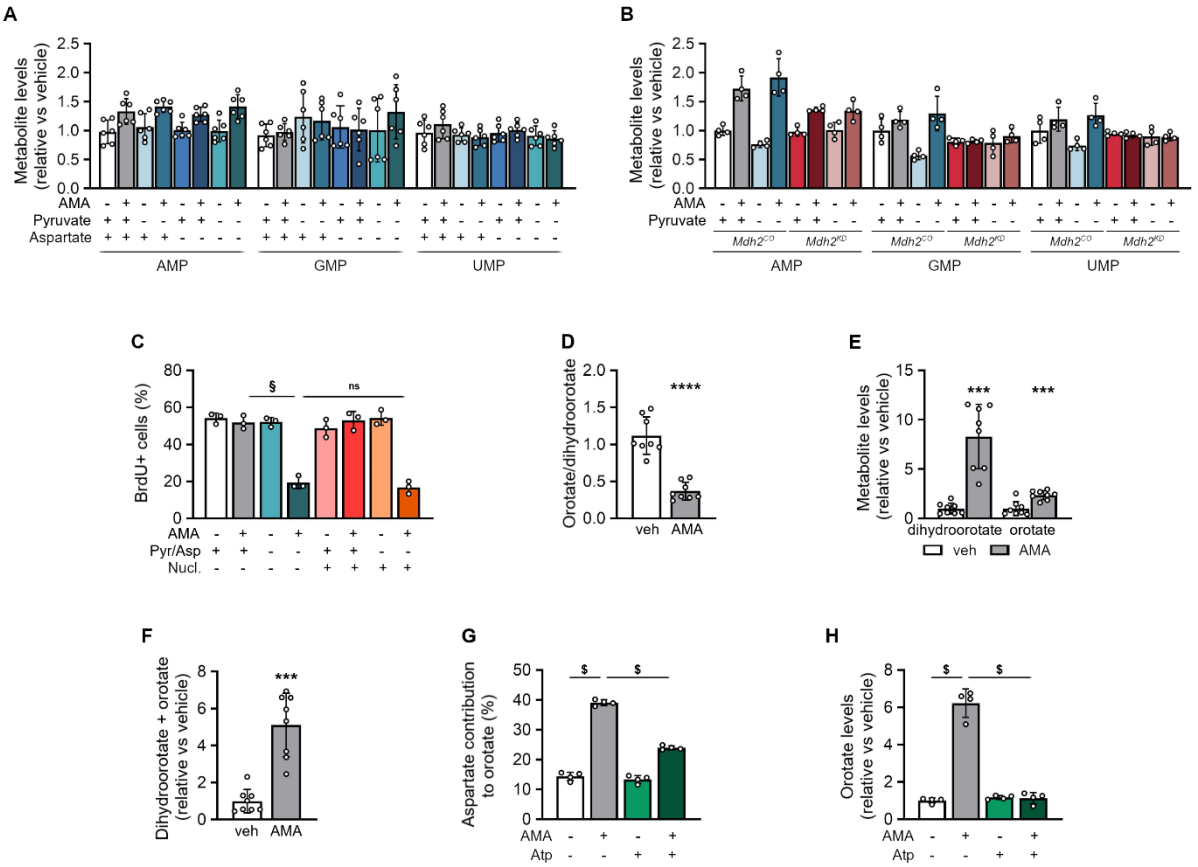

Figure S6. DHODH activity is preserved allowing pyrimidine synthesis, related to Figure 3.
(A and B) AMP, GMP and UMP levels in cells treated with vehicle (veh; control) or 10μM Antimycin A (AMA), cultured in medium with 1mM pyruvate and 0.22mM aspartate or without pyruvate and/or aspartate (A; n=6) or in veh- and AMA-treated cells transduced with control (*Mdh2*^{CO}) or MDH2-specific shRNA (*Mdh2*^{KD}) and cultured with or without pyruvate (B; n=4).
(C) Flow cytometry analysis of BrdU positive (BrdU^{+}) cells, treated with veh or AMA and cultured in full or pyruvate/aspartate (Pyr/Asp)-deprived medium supplemented or not with nucleosides (Nucl. n=3).
(D-F) Orotate to dihydroorotate ratio (D; n=8), dihydroorotate and orotate levels (E; n=8) and dihydroorotate + orotate pool (F; n=8) in veh (control)- and AMA-treated cells.
(G and H) Fractional contribution of $^{13}C_4$-aspartate to orotate (H; n=4) and orotate levels (I; n=4) in cells treated with veh (control), 10μM AMA and/or 500nM Atpenin A5 for 3 days.
Data are means ± SD. ***p<0.001, ****p<0.0001 vs veh (paired two-tailed Student's *t*-test), ns is not significant; $^{\$}$p<0.05 (two-way ANOVA), §p<0.05 (three-way ANOVA).

Figure S7

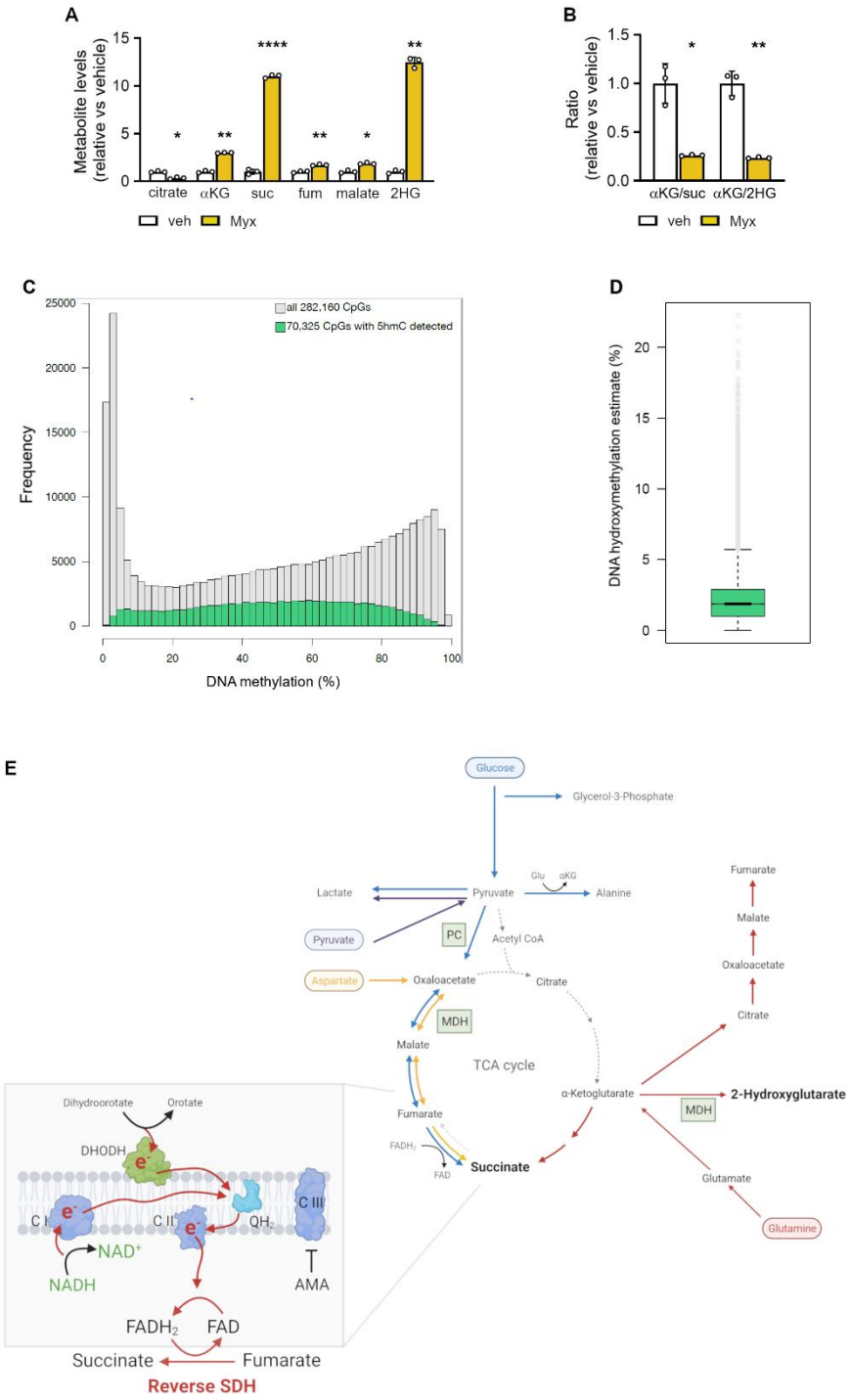
A
Metabolite levels (relative vs vehicle)
citrate
αKG
suc
fum
malate
2HG
veh
Myx
B
Ratio (relative vs vehicle)
αKG/suc
αKG/2HG
C
all 282,160 CpGs
70,325 CpGs with 5hmC detected
Frequency
DNA methylation (%)
D
DNA hydroxymethylation estimate (%)
E
Glucose
Glycerol-3-Phosphate
Lactate
Pyruvate
Alanine
PC
Acetyl CoA
Aspartate
Oxaloacetate
Citrate
MDH
Malate
TCA cycle
Fumarate
α-Ketoglutarate
2-Hydroxyglutarate
Succinate
Glutamate
Glutamine
Dihydroorotate
Orotate
DHODH
C I
C II
C III
NAD+
NADH
AMA
FADH2
FAD
Reverse SDH

Figure S7: Altered metabolite levels affect DNA demethylation, related to Figure 5.
(A and B) Citrate, α-ketoglutarate (αKG) succinate (suc), fumarate (fum), malate and 2-hydroxyglutarate (2HG) levels (A; n=3) and ratios of αKG to suc and of αKG to 2HG (B; n=3) in cells treated with vehicle (veh; control) or 10μM Myxothiazol (Myx) for 3 days.
(C) Histogram showing total DNA methylation and 5hmC signal among all 282,160 CpGs investigated.
(D) 5hmC levels in the 70,325 CpGs showing a 5hmC signal.
(E) Schematic representation of the metabolic adaptations upon ETC inhibition that result in increased levels of succinate and 2HG relative to αKG, which may induce TET activity that results in preservation of SSPC properties. Glutamine-derived αKG is converted to 2HG by malate dehydrogenase (MDH) or metabolized in the TCA cycle to succinate. Succinate cannot be further converted to fumarate as succinate dehydrogenase (SDH) is indirectly blocked by ETC complex III inhibition. Glucose-derived pyruvate enters the TCA cycle via pyruvate carboxylase (PC) and is further converted by MDH to malate and then by reverse SDH to succinate. Aspartate is also converted to succinate by the same pathway.
Data are means ± SD. *p<0.05, **p<0.01, ****p<0.0001 vs veh (two-tailed Student's *t*-test).

Table S1: List of chemicals. Related to STAR Methods: cell culture, treatment conditions.

Compounds	Supplier	Catalog number	Concentration
AKB	Sigma-Aldrich	Cat# K401	1mM
Antimycin A	Sigma-Aldrich	Cat# A8674	10µM
Aspartate	Sigma-Aldrich	Cat# A9256	0.2mM
Atpenin A5	Enzo	Cat# ALX-380-313	500nM
FK866	Sigma-Aldrich	Cat# F8557	10nM
L-Ascorbic Acid	Sigma-Aldrich	Cat# A4544	0.5mM
Myxothiazol	Sigma-Aldrich	Cat# T5580	10µM
Nucleoside mixture	merck millipore	Cat# ES-008-D	x1
Cytidine	-	-	0.73g/L
Guanosine	-	-	0.85g/L
Uridine	-	-	0.73g/L
Adenosine	-	-	0.8g/L
Thymidine	-	-	0.24g/L
Pyruvate	Gibco	Cat# 11360-039	1mM

Table S2: List of oligonucleotides. Related to STAR Methods: RNA extraction and qRT-PCR.

Short hairpins sequences			
gene	**Sequence**		
sh*Mdh2*	CCGGCGGAATGCACTTACTTCTCTACTCGAGTAGAGAAGTAAGTGCATTCCGTTTTTG		
qRT-PCR primers			
gene	**forward primer**	**probe**	**reverse primer**
Alp	CGCACGCGATGCAACA	CACTCAGGGCAATGAGGTCACATCCA	CGGACTTCCCAGCATCCTT
Coll1a1	TGTCCCAACCCCCAAAGAC	ACGTATTCTTCCGGGCAGAAAGCACA	CCCTCGACTCCTACATCTTCTGA
Coll2a1	AGAACATCACCTACCACTGTAAGAACA	CCTTGCTCATCCAGGGCTCCAATG	TGACGGTCTTGCCCCACTT
Mdh2	GAAGGAGTCGTTGAGTGTTCTT	-	CCAATGCCCAGGTTCTTCT
Nampt	TGG TTA CAG AGG AGT CTC TTC G	-	AAG CCG TTA TGG TAC TGT GC
Pcx	TGAGGCTCCTGGGTGTC	-	GATGGCAATCTCACCTCTGTT
Pparγ	CCCAATGGTTGCTGATTACAAA	CTGAAGCTCCAAGAATACCAAAGTGCGATC	AATAATAAGGTGGAGATGCAGGTTCT
Runx2	TACCAGCCACCGAGACCAA	CTTGTGCCCTCTGTTGTAAATACTGCTTGCA	AGAGGCTGTTTGACGCCATAG
Sox9	TCTGGAGGCTGCTGAACGA	CAGCACAAGAAAGACCACCC	TCCGTTCTTCACCGACTTCCT
Tet1	CAGCCGTTGAAATACATGCTC	-	ACATCCCACAGACCGAAGA
Tet2	AGAGCCTCAAGCAACCAAAA	-	ACATCCCTGAGAGCTCTTGC
Tet3	CCTTTTCTCCATACCGATCCTC	-	GAGTTCCCTACCTGCGATTG

Table S3: List of antibodies used for immunofluorescence and flow cytometry analysis. Related to STAR Methods: Western blot, Flow cytometry analysis and cell sorting.

	Antigen/reagent	Host	Conjugate	Supplier	Catalog number	Dilution
Primary antibodies	5hmc	Rabbit	-	Active Motif	39769	1/10000
	AMPKα	Rabbit	-	Cell Signaling Technology	2532	1/1000
	β-actin	Mouse	-	Sigma-Aldrich	A5441	1/10000
	BP1	Rat	PE	eBioscience	12-5891-81	1/200
	CD31	Rat	-	BD Biosciences	550274	1/50
	CD31	Rat	APC	eBioscience	17-0311-80	1/500
	CD45	Rat	APC	eBioscience	17-0451-83	1/500
	CD51	Rat	Biotin	eBioscience	13-0512-82	1/200
	CD90.2	Rat	PE	eBioscience	12-0903-81	1/200
	CD105	Rat	PE	eBioscience	12-1051-81	1/40
	CD200	Rat	PerCP-eFluor 710	eBioscience	46-5200-82	1/200
	HIF1α	Rabbit	-	Novus Biologicals	NB100-449	1/1000
	GFP	Rabbit	-	Invitrogen	A11122	1/200
	Histone H3	Rabbit	-	Cell Signaling Technology	4499	1/2000
	Histone H3 (di methyl K9)	Rabbit	-	Abcam	ab176882	1/1000
	Histone H3 (tri methyl K27)	Rabbit	-	Abcam	ab192985	1/1000
	Histone H3 (di methyl K79)	Rabbit	-	Abcam	ab3594	1/1000
	Lamin A/C	Goat	-	Santa Cruz	sc-6215	1/1000
	Mdh2	Rabbit	-	Abcam	ab96193	1/1000
	Osterix	Rabbit	-	Santa Cruz	sc-22536-R	1/10000
	PC	Rabbit	-	Invitrogen	PA5-50101	1/1000
	Phospho-AMPKα	Rabbit	-	Cell Signaling Technology	2535	1/1000
	Ter119	Rat	APC	eBioscience	17-5921-83	1/200
Secondary antibodies	anti-Goat	Rabbit	HRP	Dako	P0160	1/5000
	anti-Mouse	Rabbit	HRP	Dako	P0161	1/5000
	anti-Rabbit	Goat	Alexa 546	Invitrogen	A11010	1/200
	anti-Rabbit	Goat	Alexa 488	Invitrogen	A11008	1/200
	anti-Rabbit	Goat	HRP	Dako	P0448	1/5000
	anti-Rat	Goat	Biotin	BD Biosciences	559286	1/100
	Streptavidin	-	PE-Cyanine7	eBioscience	25-4317-82	1/200